

Effect of initial Rayleigh mode on drop deformation and breakup under impulsive acceleration

Aditya Parik^{1†}, Sandip Dighe², Tadd Truscott², and Som Dutta^{1‡}

¹Department of Mechanical and Aerospace Engineering,
Utah State University, UT 84321, USA

²Department of Mechanical Engineering,
King Abdullah University of Science and Technology, Saudi Arabia

(Received xx; revised xx; accepted xx)

One of the fundamental ways of representing a droplet shape is through its Rayleigh-mode decomposition, in which each mode corresponds to a distinct surface-energy content. The influence of these modes on free oscillation dynamics has been studied extensively; however, their role in droplet deformation, breakup, and fragmentation under impulsive acceleration remains largely unexplored. Here we systematically quantify how prescribed initial axisymmetric Rayleigh modes affect the deformation and breakup of an impulsively accelerated drop. Using experimentally validated, VOF-based multiphase direct numerical simulations, we isolate the coupled effects of finite-amplitude surface oscillation modes and the associated initial surface-energy state by initializing drops with well-defined $(n, 0)$ modes (and phases) while conserving volume at finite amplitudes. We show that breakup is governed not simply by the initial drag of the imposed shape, but by the dynamic coupling between the free modal oscillations and the forced aerodynamic (or shear-driven) deformation: constructive superposition can strongly amplify deformation, whereas destructive superposition can stabilize the drop even under otherwise disruptive forcing. Across all systems studied, the outcome is controlled by how efficiently the external work is partitioned into recoverable oscillatory energy versus centre-of-mass translation and viscous dissipation, with viscosity and density ratio acting as key mediators that respectively damp modal interactions and restrict the time window for energy uptake.

Key words: Drop deformation, impulsive acceleration, Rayleigh modes

1. Introduction

Drop deformation and fragmentation under impulsive acceleration are fundamental phenomena in processes ranging from raindrop breakup in clouds to fuel atomization in engines and agricultural spraying. Understanding the underlying physics of this process is crucial for controlling these applications.

The fragmentation process is governed by a critical threshold, first proposed by Hinze (1955) as a critical Weber number (We) for drops in turbulent flows. This concept was refined by Hsiang & Faeth (1995), who established its functional dependence on the Ohnesorge number (Oh_d). Analytical models for this critical Weber number (We_{cr}) were

† Email address for correspondence: aditya.parik@usu.edu

‡ Email address for correspondence: som.dutta@usu.edu

later developed, starting with inviscid drops [Villermaux & Bossa \(2009\)](#) and progressively extending to viscous, high-density-ratio systems [Kulkarni & Sojka \(2014\)](#); [Jackiw & Ashgriz \(2021\)](#) and the full relevant parameter space [Parik *et al.* \(2025\)](#).

Dimensional analysis shows that the dynamics of a spherical fluid drop (density ρ_d , viscosity μ_d , diameter D) impulsively accelerated by an ambient fluid (density ρ_o , viscosity μ_o , velocity V_0) are governed by the non-dimensional set $\{\rho, Oh_o, Oh_d, We_0\}$ [Parik *et al.* \(2025\)](#). The initial Weber number, $We_0 = \rho_o V_0^2 D / \sigma$, represents the ratio of disruptive aerodynamic pressure forces to restorative surface tension forces. The density ratio, $\rho = \rho_d / \rho_o$, measures the drop's inertia relative to the ambient fluid. The drop Ohnesorge number, $Oh_d = \mu_d / \sqrt{\rho_d \sigma D}$, and ambient Ohnesorge number, $Oh_o = \mu_o / \sqrt{\rho_o \sigma D}$, relate viscous and capillary timescales for the drop and ambient fluid, respectively. A Π -group representing drop deformation (and thus the closeness to fragmentation) is given by:

$$\Pi = F(\rho, Oh_o, Oh_d, We_0). \quad (1.1)$$

However, a critical assumption in this functional relationship is that the drop is initially perfectly spherical. This is rarely valid in practice. Drops in nature or industry are typically products of a primary fragmentation (e.g., from a jet or sheet), which subsequently undergo secondary fragmentation. This formation process imparts both a distorted initial shape and a complex internal velocity field. Consequently, secondary drops begin not in a static spherical state but in a dynamic state of shape oscillations, often as a superposition of many modes.

One of the earliest works to quantify drop deformation was that of [Rayleigh \(1879\)](#), who discovered that infinitesimal perturbations can exist on the surface of an inviscid drop in the form of various fundamental oscillation modes. Each mode, described by a mode number n , has a characteristic frequency ω_n dependent on surface tension σ , density ρ_d , and diameter D :

$$\omega_n^2 = \frac{8n(n-1)(n+2)\sigma}{\rho_d D^3} \quad (1.2)$$

The corresponding radial function that describes the shape of the drop $r_{n,m}$ for a given mode (n, m) , amplitude A , and phase $\psi = \omega_{n,m} t + \psi_0$, can be described using associated Legendre functions $P_{n,m}$:

$$r_{n,m}(t, \theta, \phi) = \frac{D}{2} + A \cos(\psi) P_{n,m}(\cos \theta) \cos(m\phi) \quad (1.3)$$

These oscillation modes are also known as spherical harmonics in the context of quantum mechanics, and we borrow vocabulary from that field to describe the geometry. n controls the overall complexity of the oscillation, such as the maximum number of poles, their size (i.e., wavelength of oscillation), and their characteristic oscillation frequency.

For each fundamental mode n , there exist $0 \leq m \leq n$ unique auxiliary or harmonic modes that display differing orientations. For a drop undergoing free oscillations of small amplitudes, these modes are degenerate, i.e., the oscillation frequency is exactly the same for all m . However, this degeneracy is broken for highly deformed drops or those under the action of external forces. Figure 1 shows the three harmonic modes for $n = 2$. The $m = 0$ mode is axisymmetric and is also described as a “zonal” mode, resulting from a stretching or flattening along the z -axis. The $m = 1$ and $m = 2$ modes, on the other hand, are non-axisymmetric. The $m = 1$ mode (“tesseral”) results from a twist or shear, while the $m = 2$ mode (“sectoral”) produces 4 lobes deforming into the equatorial plane.

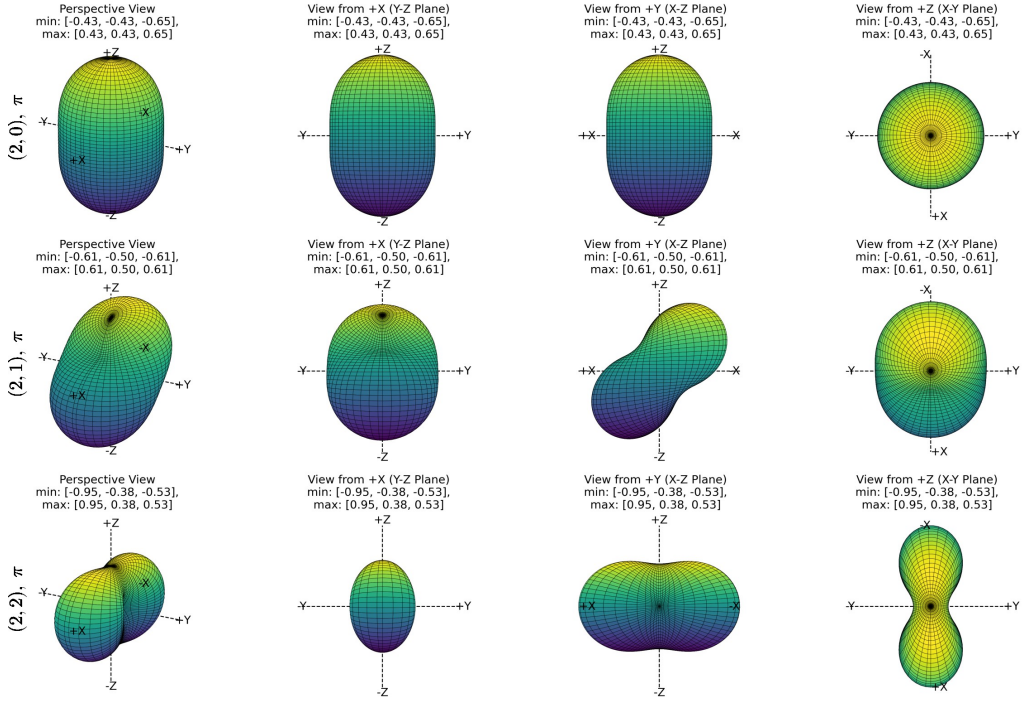


Figure 1: The harmonic modes for the fundamental oscillation $n = 2$ at an extreme phase. The $(2, 0)$ “zonal” mode is axisymmetric, while the $(2, 1)$ “tesseral” and $(2, 2)$ “sectoral” modes are non-axisymmetric.

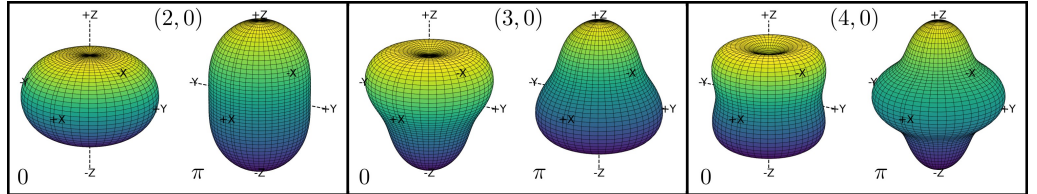


Figure 2: The figure shows 3-dimensional renders of the two extreme deformation phases, 0 and π , for the $(2, 0)$, $(3, 0)$, and $(4, 0)$ axisymmetric Rayleigh oscillation modes, which are the focus of the current study.

This concept of the $(n, 0)$ mode being “zonal”, the (n, n) mode being “sectoral”, and all other harmonics showing “tesseral” geometry exists for all fundamental modes.

In this work, we focus exclusively on the axisymmetric “zonal” modes ($m = 0$), as they represent a primary deformation relevant to the axisymmetric forcing. The specific modes under investigation, $(2, 0)$, $(3, 0)$, and $(4, 0)$, are illustrated in Figure 2.

Subsequent work on drop oscillations revealed a far more complex picture. Viscosity, while classically known to damp oscillations (Lamb (1932); Chandrasekhar (1959)), was found to have a profound and non-trivial impact on the dynamics. It strongly influences mode coupling, causing higher modes to damp more quickly Meradji *et al.* (2001) and significantly enhancing resonant interactions between modes Basaran (1992); Becker *et al.* (1994). Furthermore, for amplitudes exceeding $\sim 10\%$ of the drop radius, nonlinear effects dominate Becker *et al.* (1991), including a characteristic decrease in oscillation frequency

with increasing amplitude Brant Foote (1973); Trinh & Wang (1982) and an asymmetry in the oscillation period Trinh & Wang (1982); Tsamopoulos & Brown (1983). Most recently, Zrnić *et al.* (2022) found that even a second-order nonlinear approximation captures the frequency decrease in viscous drops, in contrast to the inviscid case Zrnić & Brenn (2021). Viscosity was also shown to enhance mode coupling, which preferentially transfers energy from higher modes to the fundamental $n = 2$ mode. The internal velocity field (kinetic energy) imparted during formation can be as significant as the initial surface energy (potential energy) Zhang *et al.* (2019). This initial internal circulation can amplify oscillation amplitudes, induce phase shifts, and cause significant energy transfer between modes. Thus, a “non-spherical” drop is a complex dynamic system with a pre-existing energy state that dictates its subsequent evolution.

Despite this rich understanding of free oscillations, research on initially deformed drops under external forcing is scarce, and has focused primarily on drops falling under gravity Szakáll *et al.* (2009, 2010); Agrawal *et al.* (2017, 2020); Balla *et al.* (2019). To our knowledge, no systematic work has explored how a drop with a well-defined initial oscillation mode behaves under an instantaneous force loading, characteristic of impulsive acceleration.

The coupling between aerodynamic forcing and drop shape oscillations can be significant, as the aerodynamic deformation timescale (τ_D) and the Rayleigh oscillation period ($2\pi/\omega_n$) can be of the same order of magnitude, particularly for the fundamental $n = 2$ mode. For an integer N , this can be expressed as

$$\tau = \frac{D\sqrt{\rho}}{V_0} \sim N \frac{2\pi}{\omega_n}. \quad (1.4)$$

This temporal proximity suggests that the “natural” oscillations from the initial shape can appreciably interact with the “forced” deformation from the aerodynamic load. This interaction could be constructive, amplifying deformation, or destructive, stabilizing the drop. The drop’s initial energy state effectively alters the starting point for the fragmentation process. We expect drop viscosity (Oh_d) to be a key mediator, damping the initial oscillations and thus controlling the magnitude of this interaction.

In the current paper, we quantify the effect of this initial modal shape and its associated energy on the subsequent deformation, internal flows, and overall energetics. We use the modal definition of Rayleigh (1879) to systematically define initial shapes and employ VOF-based direct numerical simulations to analyze the resulting drop dynamics.

2. Problem Description and Model Formulation

2.1. Problem definition

As described in section 1, a drop-ambient system under impulsive acceleration is completely characterized by the non-dimensional set $\{\rho, Oh_o, Oh_d, We\}$. Parik *et al.* (2025) found that the threshold is strongly dependent on all three of the parameters, with We_{cr} achieving values from 10 (for water-air like systems) to 70 (for $\rho \sim 10$ systems). Non-trivial morphologies are also observed, such as forward pancakes for low density low Reynolds number systems, and large drop viscosity is found to suppress plume formation (due to its high viscous dissipation).

In order to efficiently study the effect of initial drop shape on the drop deformation and breakup, we will consider a representative subset of $\{\rho, Oh_o, Oh_d, We\}$, that may capture the wide variety of deformation characteristics observed in Parik *et al.* (2025). More specifically, the following three representative cases are chosen to represent the range of possible deformation characteristics:

- (i) A water drop impulsively accelerated in air at its threshold conditions; this is the most common scenario in nature and industry, and hence is a good benchmark case;
- (ii) Impulsive acceleration of a Newtonian liquid 100 times more viscous than water; a representative case for systems such as retardant fluids used in aerial firefighting;
- (iii) A water drop impulsively accelerated in another liquid with densities and viscosities in the same order of magnitude, representative of a liquid-liquid system.

A water drop impulsively accelerated in air at threshold conditions is defined by the following non-dimensional parameters: $\rho = 815.92$, $Oh_d = 1.258 \times 10^{-3}$, $Oh_o = 6.96 \times 10^{-4}$, and $We = 12$. The non-dimensional numbers for the other two drop-ambient systems will be defined relative to the water-air system. For the three cases listed above, we will impose three different initial axisymmetric oscillation modes on the drop: (2, 0), (3, 0), and (4, 0), using a corrected form of the general Rayleigh description of sinusoidal surface oscillations described by equation 1.3. The corrected form is given by equation 2.2 used with equation 2.4, and will be described in section 2.2. For each mode, two different initial phases ϕ will be considered such that the influence of starting at any of the two extreme states of the oscillation mode is studied. The prolate shape observed in the experiments in 2.5 can be approximated as a (2, 0) Rayleigh mode oscillation with an amplitude of $A \approx 0.3$, and will be set as the oscillation amplitude for all simulations conducted in this work. Figure 4(b) shows an illustration (to scale) of the three modes and the two initial phases of amplitude 0.3 imposed on a sphere of diameter 1.

All the cases considered in this work are summarized in the table 1 with the final column specifying a **case** ID for every case. We will use the **case** IDs to easily reference the cases in all subsequent text.

2.2. Finite-amplitude correction for the Rayleigh oscillation modes

For this work, we focus on generating initial drop shapes using axisymmetric Rayleigh modes, corresponding to the $(n, 0)$ modes in the equation 1.3. At time $t = 0$, the shape is a superposition of these modes:

$$r_n(\theta) = R_0 + \sum_{n=2}^{n \rightarrow \infty} A_n P_n(\cos \theta) \quad (2.1)$$

Here, R_0 is the radius of the unperturbed sphere, A_n is the amplitude of the n^{th} mode, and P_n is the associated Legendre polynomial.

However, this classical formulation, derived under the assumption of infinitesimally small perturbations, has a critical limitation: it fails to conserve the volume of the drop at finite amplitudes. As shown in figure 3, applying Rayleigh modes with large amplitudes to a sphere results in a drop shape with a significantly greater volume than the original sphere. Maintaining the same Weber number and total drop inertia, both directly proportional to the volume-averaged diameter of the drop, across all comparable simulations is paramount. This discrepancy in the volume of the drop (and thus its effective Weber number) thus makes the standard Rayleigh shape description unsuitable for initializing the current simulations.

This discrepancy can be corrected by reintroducing the previously omitted $n = 0$ mode, which represents a uniform change in the base radius of the drop over which all oscillation modes are superposed. The general form of the shape equation is thus modified to include this term:

$$r_n(\theta) = b_0 + \sum_{n=2}^{n \rightarrow \infty} A_n P_n(\cos \theta) \quad (2.2)$$

Drop-Ambient System	ρ	Oh_o	Oh_d	We	A_0	n	ϕ	Case ID
Water Drop in Air	815.92	6.96×10^{-4}	1.26×10^{-3}	12	0.3	2	0	WA20
	815.92	6.96×10^{-4}	1.26×10^{-3}	12	0.3	2	π	WA2P
	815.92	6.96×10^{-4}	1.26×10^{-3}	12	0.3	3	0	WA30
	815.92	6.96×10^{-4}	1.26×10^{-3}	12	0.3	3	π	WA3P
	815.92	6.96×10^{-4}	1.26×10^{-3}	12	0.3	4	0	WA40
	815.92	6.96×10^{-4}	1.26×10^{-3}	12	0.3	4	π	WA4P
High Viscosity Drop in Air	815.92	6.96×10^{-4}	1.26×10^{-1}	18	0.3	2	0	HA20
	815.92	6.96×10^{-4}	1.26×10^{-1}	18	0.3	2	π	HA2P
	815.92	6.96×10^{-4}	1.26×10^{-1}	18	0.3	3	0	HA30
	815.92	6.96×10^{-4}	1.26×10^{-1}	18	0.3	3	π	HA3P
	815.92	6.96×10^{-4}	1.26×10^{-1}	18	0.3	4	0	HA40
	815.92	6.96×10^{-4}	1.26×10^{-1}	18	0.3	4	π	HA4P
Water Drop in Another Liquid	10.0	1.26×10^{-3}	1.26×10^{-3}	10	0.3	2	0	LL20
	10.0	1.26×10^{-3}	1.26×10^{-3}	10	0.3	2	π	LL2P
	10.0	1.26×10^{-3}	1.26×10^{-3}	10	0.3	3	0	LL30
	10.0	1.26×10^{-3}	1.26×10^{-3}	10	0.3	3	π	LL3P
	10.0	1.26×10^{-3}	1.26×10^{-3}	10	0.3	4	0	LL40
	10.0	1.26×10^{-3}	1.26×10^{-3}	10	0.3	4	π	LL4P

Table 1: All drop-ambient systems simulated for this study are presented in this table. A “case ID” is specified for each case for each initial mode and phase for easy reference in the text.

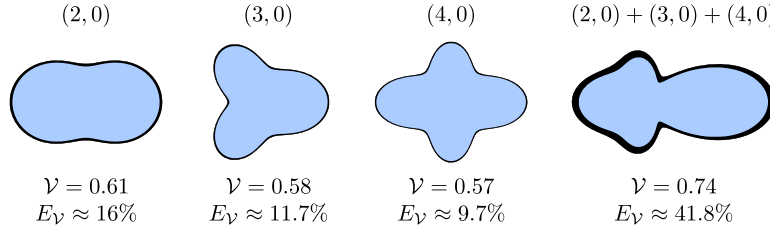


Figure 3: The original Rayleigh mode description fails to conserve the volume of the drop for non-infinitesimal amplitudes, resulting in a drop with a volume greater than the volume of the parent sphere. This error in drop shape and subsequent increase in drop volume is represented by the black outer region for each case, while the light blue inner region represents the drop shape corrected using equations 2.2 and 2.4. All four drops result from the uncorrected Rayleigh modes on a sphere of diameter $D = 1$ (volume is $\pi/6 \approx 0.523$). $A = 0.5$ is the amplitude of the Rayleigh mode(s), V is the volume of the deformed drop, and E_V is the error in the volume of the deformed drop.

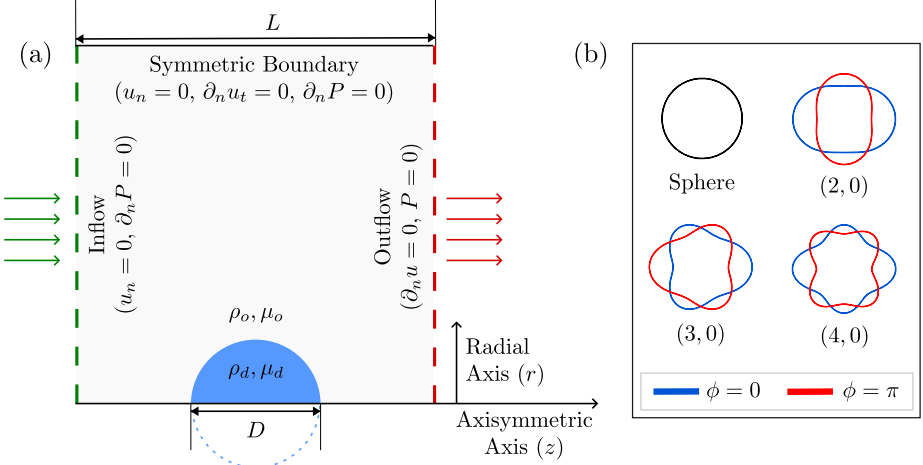


Figure 4: (a) The computational domain for the problem under consideration. (b) The three oscillation modes and the corresponding two initial phases of amplitude 0.3 imposed on a sphere of diameter 1.

where $b_0 = R_0 + A_0$ is a corrected base radius that is no longer equal to R_0 for finite amplitudes. To find the value of b_0 that ensures volume conservation, we begin by equating the volume of the original spherical drop to the volume of the deformed drop by integrating the shape equation over 0 to π :

$$\frac{4}{3}\pi R_0^3 = \frac{2\pi}{3} \int_{\theta=0}^{\pi} [r_n(\theta)]^3 \sin \theta \, d\theta \quad (2.3)$$

By substituting the corrected shape equation 2.2 into this volume integral and performing the integration (detailed in the Appendix), we arrive at the final cubic equation for the corrected non-dimensionalized base radius, $\tilde{b}_0 (= b_0/R_0)$:

$$1 = 8\tilde{b}_0^3 + 24\tilde{b}_0 \sum_{n=2}^{n \rightarrow \infty} \frac{\tilde{A}_n^2}{2n+1} + 8 \sum_{i,j,k}^{\infty} \tilde{A}_i \tilde{A}_j \tilde{A}_k \begin{pmatrix} i & j & k \\ 0 & 0 & 0 \end{pmatrix}^2 \quad (2.4)$$

This equation can be readily solved for \tilde{b}_0 using a standard numerical root-finding algorithm given $0 < \tilde{b}_0 \leq 0.5$. Using the obtained \tilde{b}_0 in equation 2.2 provides an initial drop geometry that perfectly conserves the volume for any arbitrary superposition of axisymmetric Rayleigh modes at any amplitude.

2.3. Governing Equations and Solver

The simulations are performed using the open-source solver Basilisk Popinet (2003, 2009), which is extensively validated for two-phase flows Popinet & Zaleski (1999); Popinet (2003, 2009, 2015); van Hooft *et al.* (2018); Farsoiya *et al.* (2021). Basilisk solves the incompressible two-phase Navier-Stokes equations using a one-fluid formulation:

$$\rho(\partial_t \mathbf{u} + \mathbf{u} \cdot \nabla \mathbf{u}) = -\nabla p + \nabla \cdot (2\mu \mathbf{D}) + \sigma \kappa \delta_s \mathbf{n}, \quad (2.5a)$$

$$\nabla \cdot \mathbf{u} = 0 \quad (2.5b)$$

where \mathbf{u} is the fluid velocity, ρ is the density, μ is the dynamic viscosity, p is the pressure, and \mathbf{D} is the deformation tensor ($D_{ij} = (\partial_i u_j + \partial_j u_i)/2$). Surface tension is modeled as a body force using a Continuum Surface Force (CSF) approach Brackbill

et al. (1992). The δ_s function applies this force only at the interface, where σ is the surface tension coefficient, and κ and \mathbf{n} are the interface curvature and normal. A balanced-force formulation and height-function-based curvature estimation are employed to minimize parasitic currents Francois *et al.* (2006); Popinet (2009).

The one-fluid model defines local properties based on the volume fraction $c(\mathbf{x}, t)$ of one fluid (e.g., the drop, ρ_d, μ_d) relative to the other (e.g., the ambient, ρ_o, μ_o):

$$\rho = c \rho_d + (1 - c) \rho_o, \quad (2.6a)$$

$$\mu = c \mu_d + (1 - c) \mu_o \quad (2.6b)$$

The interface is tracked by advecting the volume fraction field c using a geometric VOF method:

$$\partial_t c + \nabla \cdot (c \mathbf{u}) = 0 \quad (2.7)$$

The solver utilizes a quadtree-based adaptive mesh, which dynamically refines the grid at the fluid interface, enabling high-resolution capture of capillary phenomena at a reduced computational cost. For a more detailed description of the numerical methods and implementation, we refer the reader to Popinet (2003, 2009).

2.4. Computational setup and initial conditions

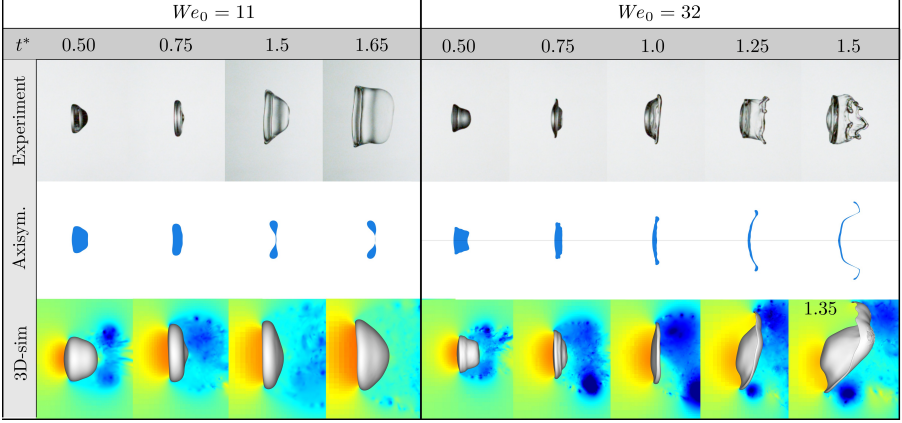
Given that the primary deformation process is predominantly axisymmetric Parik *et al.* (2025) and our focus is on axisymmetric initial modes ((n, m) with $m = 0$), we utilize axisymmetric simulations. The computation is carried out in an axisymmetric square domain of size L , as illustrated in figure 4(a). The domain size L is set to $16D$ for high-inertia drops ($\rho \geq 100$) and $32D$ for low-inertia drops ($\rho = 10$) to ensure that the drop remains a sufficient distance from the boundaries.

The left boundary is a uniform inflow ($u_n = V_0 = 1$), the right boundary is a free outflow ($\partial_n u_n = 0$), the bottom boundary is the axis of symmetry, and the top boundary is a symmetric boundary. At $t = 0$, the drop (with a volume-averaged diameter $D = 1$) is initialized with zero velocity. While our previous work Parik *et al.* (2025) focused on an initially spherical drop, the current study imposes initial non-spherical shapes. These shapes correspond to the $(2, 0)$, $(3, 0)$, and $(4, 0)$ axisymmetric Rayleigh modes with an initial amplitude of $A = 0.3$, as detailed in section 2.1 and illustrated in figure 4(b).

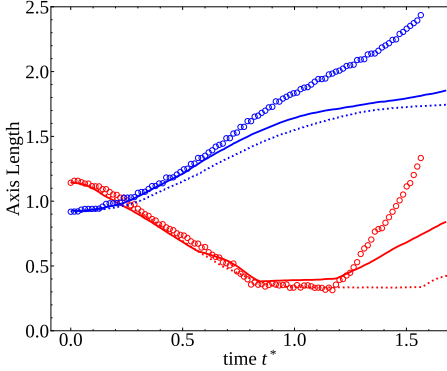
The solution accuracy is controlled by the wavelet error thresholds for the velocity (χ_u) and volume fraction (χ_c) fields, the tolerance of the Poisson solver (ϵ_p), and the maximum refinement level (N). Based on the detailed convergence study presented in our previous work Parik *et al.* (2025), we use the following converged parameters for all simulations: 1) Wavelet error for velocity $\chi_u = 10^{-4}$, 2) Wavelet error for volume fraction $\chi_c = 10^{-6}$, and 3) Poisson solver residual $\epsilon_p = 10^{-4}$. The minimum allowed cell size is set to 1024 cells per diameter ($N = 14$ for $L = 16$) for all cases. Finally, some energy and dissipation metrics are derived from the simulations and are described in section 4. It is essential that we test that these higher order metrics are also converged for the simulation parameters chosen for all the cases in order to ensure their voracity. We present this test in appendix C.

2.5. Comparison of axisymmetric simulations against 3D simulations and experiments

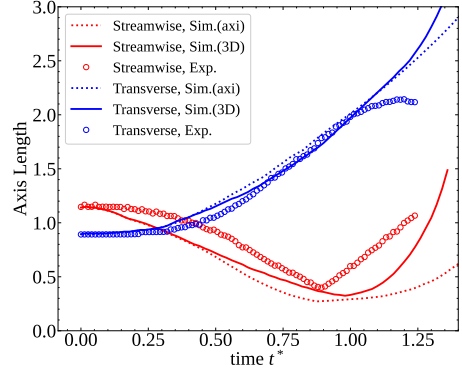
The numerical framework used in this study, based on axisymmetric simulations in Basilisk, was extensively verified in Parik *et al.* (2025). In that work, the solver's performance was benchmarked against the canonical bag breakup experiment of Flock *et al.* (2012), with results compared to both the experimental data and recent experiments



(a) Drop snapshots for two different wind tunnel velocities (i.e., two different Weber numbers) for different non-dimensional times is shown, along with the corresponding axisymmetric and 3D VOF field renders from the simulations.



(b) Axis lengths for $We = 11$.



(c) Axis lengths for $We = 32$.

Figure 5: The impulsive acceleration of a prolate drop in a vertical wind tunnel for two different wind tunnel velocities is simulated in both axisymmetric and three-dimensions using Basilisk. Time (t^*) is scaled by the deformation timescale $\tau_D = \sqrt{\rho}(D/V_0)$, and length is scaled by the drop diameter (8 mm).

and simulations in the literature. One of the key findings of [Parik *et al.* \(2025\)](#) was that while axisymmetric simulations cannot capture late-stage dynamics and 3D phenomena such as bag rupture; they accurately model the initial deformation (at least up to the initiation time), correctly predicting the evolution of streamwise and transverse dimensions up to the formation of the critical pancake state ($t^* \approx 1.2$). This reliability was confirmed across a broad parameter space of ρ , Oh_o , and Oh_d using 3D simulations (Appendix C of [Parik *et al.* \(2025\)](#)), predicting non-trivial pancake morphologies such as forward-pancake and the subsequent inflation orientation. However, axisymmetric simulations were found to be unreliable for very low-viscosity systems ($Oh_o, Oh_d \leq 0.001$), where the ambient flow is chaotic and accompanied with extremely low viscous dissipation in the drop fluid. If the parameters chosen for the present study lie well within the verified parameter space, the axisymmetric approach can be considered appropriate. The purpose of this section is to extend this verification to the specific case of initially non-spherical (prolate) drops, which is the central focus of this work.

To this end, we compare our simulations with a new set of experiments conducted using water droplet (8 mm in diameter). The droplets are released using a custom-designed mechanism that provides precise control over their initial shape at the moment of release, thereby allowing impulsive exposure of the droplet to the air jet at a desired shape/state. Details of the experimental setup are provided in appendix B, and a schematic of the setup is shown in Figure 21. Following release, during free fall, the droplet undergoes natural oscillations. The ensuing aerodynamic deformation is systematically investigated for the prolate shape of the droplet. The air jet is activated precisely when the droplet reaches its maximum prolate deformation. This timing ensures that the droplet possesses negligible oscillatory kinetic energy at the onset of aerodynamic forcing, such that its initial condition is defined primarily by its shape, i.e., surface energy. The dimensionless parameters for this system are a density ratio of $\rho = 815.92$, a drop Ohnesorge number of $Oh_d = 1.258 \times 10^{-3}$, and an ambient Ohnesorge number of $Oh_o = 6.96 \times 10^{-4}$.

Two experiments corresponding to two different wind velocities driving the impulsive acceleration are considered, 6.65 m/s and 12.97 m/s. For the former case, the drop achieves its prolate extreme at a drop velocity of 2.33 m/s, resulting in a wind velocity relative to the drop of $V_0 \approx 9.0$ m/s. This gives us an initial Weber number $We_0 \approx 11$. The corresponding prolate initial shape has a streamwise axis length of $b = 9.136$ mm, and a transverse axis length of $a = 7.35$ mm. For the case with a wind velocity of 12.97 m/s, $V_0 \approx 15.25$ m/s, and the resulting prolate drop has $b = 9.176$ mm, $a = 7.135$ mm, and $We_0 \approx 32$. For the numerical simulations, these initial shapes are modeled as ellipsoids, with their major and minor axes aligned with the streamwise and transverse directions, respectively. Since the experimental drops are not perfect ellipsoids, discrepancies in deformation characteristics between the simulations and experiments are anticipated due to this idealization.

Figure 5 compares snapshots from these experiments with the corresponding renders from the current numerical simulations. A quantitative comparison of the drop's streamwise and transverse axis lengths is also provided. For both Weber numbers, an acceptable agreement between the experiments and the simulations is observed during the initial deformation phase, up to the formation of a pancake ($t^* \approx 1.2$). The orientation of the pancake and the subsequent inflation is correctly predicted by the simulations, as can be seen from the similar positive slope of the streamwise lengths achieved by the simulations and the experiment. Beyond this point, as the drop begins to form a bag ($We = 11$) or eject sheets from its periphery ($We = 32$), the inherently three-dimensional dynamics cause the simulation results to diverge from the experimental data, as expected.

This work aims to explore the role of initial shape of the drop on the subsequent deformation when exposed to impulsive acceleration. For the purposes of this work, we require the numerical model to allow us to at least predict the essential deformation characteristics such as the shape and orientation of the pancake, since the drop's deformation and fragmentation characteristics are primarily determined by the balance of all the forces acting on the drop (and corresponding energetics) up until this point. An accurate estimate of the final fragmentation morphology is not of interest for this work. Since the axisymmetric simulations capture the drop's evolution up to this critical stage, both for spherical (Parik *et al.* 2025) and prolate initial shapes (verified here), the numerical model is deemed sufficient for the purposes of this investigation.

3. Results

We begin by examining the macroscopic kinematics for the six initial Rayleigh shapes relative to the reference spherical case, as presented in figure 6. Figure 6a plots the

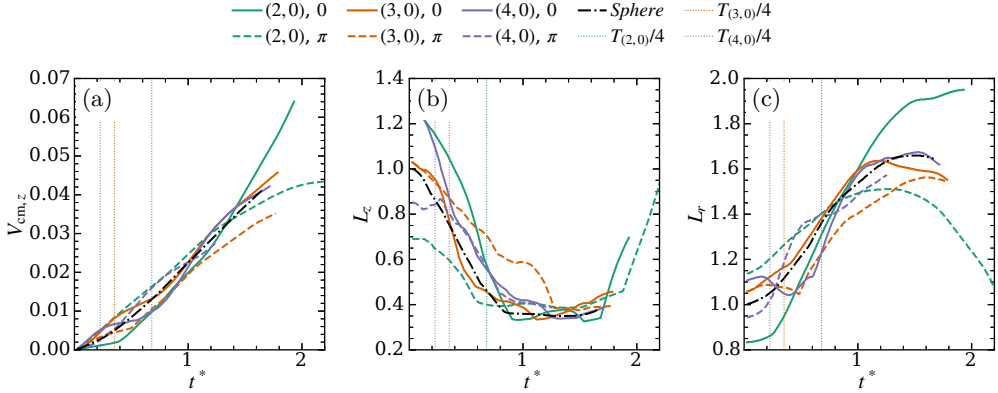


Figure 6: Temporal evolution of macroscopic kinematics and deformation metrics for a water drop impulsively accelerated in air. The panels display (a) the axial centre-of-mass velocity, $\mathbf{V}_{\text{cm},z}$; (b) the drop's streamwise axis length, L_z ; and (c) the transverse axis length, L_r , plotted against dimensionless time t^* . The results for the spherical reference case are compared against the three fundamental Rayleigh modes ($n = 2, 3, 4$) initialized at their extreme phases (0, π).

temporal evolution of the centre-of-mass velocities. Initially, the 0 phase of the (2,0) mode (WA20) exhibits the lowest centre-of-mass acceleration, achieving a $\mathbf{V}_{\text{cm},z}$ approximately one-fifth the magnitude of the π phase by $t^* \approx 0.4$. This is consistent with its aerodynamically favourable prolate shape and significantly smaller frontal area. However, at $t^* \approx 0.4$, WA20 undergoes a rapid increase in acceleration, surpassing WA2P. This transition coincides with the development of a blunt upstream face, which significantly increases aerodynamic drag.

For the (3,0) mode, the π phase is geometrically more aerodynamic than the 0 phase, yet both share a similar projected frontal area. Interestingly, during the initial stages of impulsive acceleration ($t^* < 0.2$), WA30 and WA3P exhibit nearly identical accelerations. This suggests that in the early regime where the boundary layers remain attached and flow separation has not yet occurred, the drag is dominated by viscous stresses acting on the drop's surface. Since both phases expose comparable surface areas to the flow, the net viscous forcing is similar. However, once the flow separates, the pressure drag (form drag) becomes dominant. At this stage ($t^* \approx 0.4$), the more aerodynamic WA3P experiences a lower total drag force, evidenced by the distinct reduction in the slope of its velocity curve relative to WA30. A similar trend is observed for the (4,0) mode. The 0 phase initially accelerates faster, suggesting a larger effective viscous drag during the attached-flow regime. However, as the flow fully develops, its higher aerodynamicity (due to the streamlined axial lobes) allows it to experience lower pressure drag relative to the π phase, resulting in a lower accelerations.

Notable temporal modulations in centre-of-mass acceleration ($d\mathbf{V}_{\text{cm},z}/dt$) are observed for the higher modes beyond $t^* \approx 0.4$. For instance, WA30 starts with high acceleration but shows a distinct decrease and subsequent increase in $d\mathbf{V}_{\text{cm},z}/dt$ at the quarter-period $T_{(3,0)}/4$ and half-period $T_{(3,0)}/2$, respectively. Similar periodic variations corresponding to the Rayleigh time-period are observed for WA40. This indicates that centre-of-mass acceleration is governed not merely by the static aerodynamics of the instantaneous shape, but is dynamically modulated by the oscillation mode imposed on the drop. The spherical case, lacking an imposed mode, shows no such fluctuations.

As the drops deform, the aerodynamic loading they experience evolves in complexity. While the net aerodynamic force acts strictly in the streamwise direction (drag), the *distribution* of pressure and shear stresses over the non-rigid interface performs work in both axial and radial directions. Specifically, the strong pressure gradient from the upstream pole to the periphery generates a net radial forcing on the drop fluid. Because the drop is deformable, this radial forcing performs work, effectively channeling a portion of the total aerodynamic power into radial expansion (internal oscillatory energy) rather than bulk acceleration (translational kinetic energy). Thus, differences in initial shape do not merely alter the total drag coefficient; they fundamentally modulate how the external work is partitioned between accelerating the center of mass and driving the radial deformation. WA20 exhibits a significantly higher rate of radial expansion than all other cases, achieving a larger transverse length L_r by $t^* \approx 0.8$. Despite differing initial axial and radial lengths, most cases converge to a similar radial extent of $L_r \approx 1.45$ by $t^* \approx 1.0$, highlighting that different initial shapes undergo markedly different deformation rates to arrive at a similar pancake morphology. The notable exception is WA3P, which maintains distinct L_z and L_r values for the majority of the deformation process, only converging to the common values later at $t^* \approx 1.3$.

To elucidate how the macroscopic energy partitioning described above manifests within the fluid, we must isolate the internal motion from the drop's bulk translation. Accordingly, we define an *oscillatory velocity*, $\tilde{\mathbf{V}}$, as the deviation of the local velocity field $\mathbf{V}(\mathbf{x}, t)$ from the volume-averaged centre-of-mass velocity $\mathbf{V}_{cm,z}$ (i.e., $\tilde{\mathbf{V}} = \mathbf{V} - \mathbf{V}_{cm,z}$).

Figure 7 presents the evolution of these internal velocities for the three initial shapes at various dimensionless times, t^* . The snapshots utilize pseudo-colour renders partitioned into two halves: the upper half depicts the radial component (\tilde{V}_r), whilst the lower half displays the axial component (\tilde{V}_z). The final column illustrates the drop's shape at the instant of fragmentation, where applicable. With the sole exception of the $(2, 0), \pi$ case, all initial shapes lead to fragmentation, albeit at varying times. The subsequent analysis focuses on the qualitative evolution of these internal flow patterns and their deviation from the spherical reference case.

For the $(2, 0)$ mode, a striking difference in behaviour is observed between the two initial shapes. Although WA20 is aerodynamically favourable—experiencing lower initial drag as noted in the macroscopic analysis—it exhibits significantly larger oscillatory velocities compared to the π phase. This apparent contradiction is resolved by considering the local pressure distribution rather than the net drag. Analytical descriptions of impulsive deformation (Villermaux & Bossa 2009; Kulkarni & Sojka 2014; Parik *et al.* 2025) indicate that radial expansion is driven by the pressure difference between the upstream pole and the periphery. The prolate WA20 shape possesses a high curvature at the stagnation point (pole) and low curvature at the periphery, significantly enhancing this pressure gradient relative to the spherical or oblate cases. This geometric advantage allows the $(2, 0)$ mode to channel a larger fraction of the aerodynamic work into internal flow, driving strong deformation despite the lower global drag. Conversely, WA2P displays the lowest internal velocity magnitudes of all cases and notably fails to fragment.

However, the two extreme shapes of the $(3, 0)$ mode exhibit very similar internal velocity structures, despite their differences in initial acceleration. WA30 initially deforms faster, as visible in the snapshots at $t^* \approx 0.4$, driven by the steep pressure gradients associated with its blunt frontal profile. A peak in radial velocity is observed where the prospective downstream peripheral bulge for the π phase would reside, hinting at a strong influence of the modal oscillation on the internal oscillatory velocities. Similarly, the π extreme state (WA3P) shows the highest radial velocities in the region where the upstream

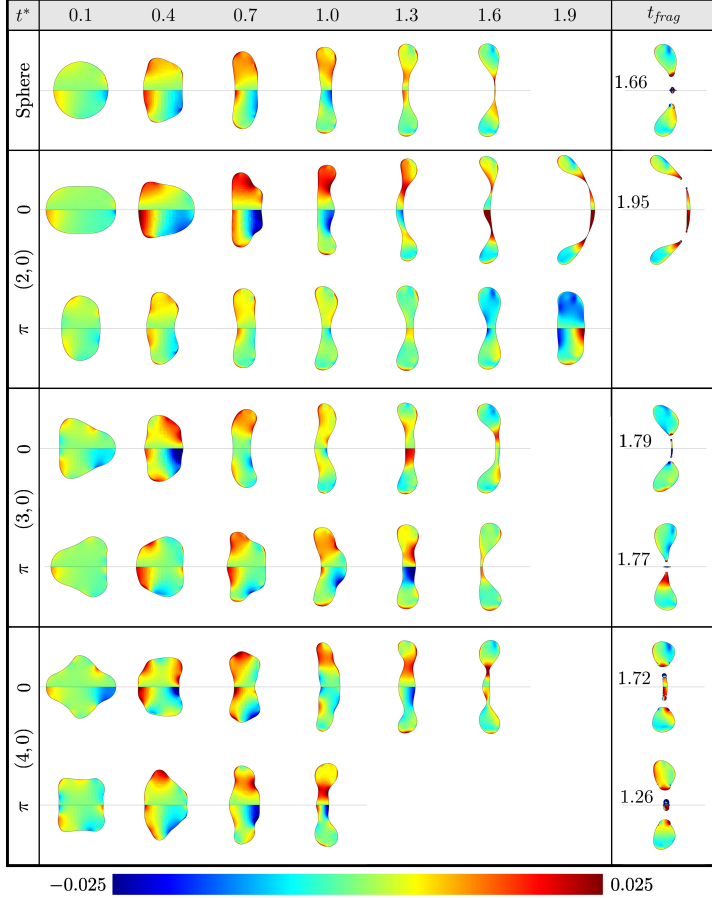


Figure 7: Temporal evolution of internal velocity fields at various t^* for water drops initialized with different shapes. The upper half of each drop depicts the radial velocity component, while the lower half displays the axial velocity component.

peripheral bulge is expected to form. A key factor here is that the half-period of the $(3, 0)$ mode is approximately 0.7, which is very close to the time the reference spherical case takes to achieve its highest radial velocities. The temporal evolution from $t^* = 0.1$ to 1.0 clearly shows both phases completing one half-cycle of their natural oscillation. By the time the drops fragment ($t_{frag}^* \approx 1.77$), the two modes have undergone at least one full oscillation cycle; consequently, the drop experiences the full range of aerodynamic advantages and disadvantages associated with both shapes.

A more drastic difference in fragmentation time is observed for the $(4, 0)$ mode drops, with the π phase fragmenting significantly earlier than the 0 phase. The natural half-period of this mode is short (approximately 0.45), implying the drop undergoes at least one full oscillation before fragmenting. The initial flow for the 0 phase, transitioning towards the π phase, is constructive to the fragmentation process as it drives fluid away from the poles. This is evident in the snapshots at $t^* = 0.7$, where both the 0 and π phase drops display features resembling their opposite extreme shapes. For WA40, the highest radial and oscillatory axial velocities are observed where the mid-latitude bulge is expected to appear during the transition to the π phase. We observe similar behaviour in WA4P, where the largest radial velocities are seen at the peripheral bulge at $t^* \approx$

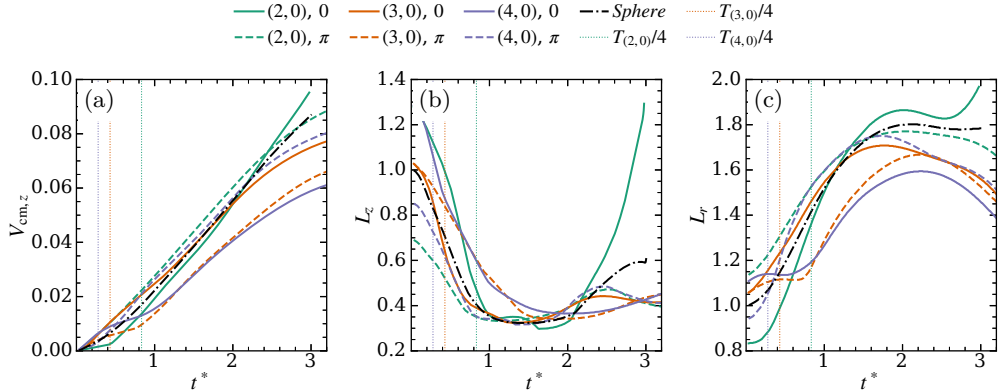


Figure 8: Temporal evolution of macroscopic kinematics for a high-viscosity drop impulsively accelerated in air. The panels display (a) the axial centre-of-mass velocity, $V_{cm,z}$; (b) the drop’s axial length, L_z ; and (c) the radial length, L_r , as functions of dimensionless time t^* . The spherical reference case is compared against the three fundamental Rayleigh modes ($n = 2, 3, 4$) initialized at their extreme phases ($0, \pi$).

0.4. By $t^* \approx 0.8$, the two cases have theoretically achieved their opposite extremes and begin deforming back towards their initial shapes. For WA4P at $t^* \approx 1$, the drop has arrived at a physical morphology that supports fragmentation. WA4O, on the other hand, is transitioning towards a shape with axial lobes at $t^* \approx 0.7$, and thus possesses kinetic energy that directly opposes bag formation. Consequently, the drop requires an additional half-period to arrive at a similar quasi-equilibrium state with significantly less oscillatory kinetic energy opposing the formation of a bag.

In contrast to the low-viscosity case, a drop comprising fluid 100 times more viscous exhibits markedly different behaviour under the same impulsive acceleration. Since the ambient Reynolds number remains comparable to the water-air system ($Re \approx 0.8Re_{\text{water}}$), the external flow physics remains governed by the transition from initial viscous shear stress to flow separation and pressure drag. We first examine the macroscopic kinematics in figure 8. Similar to the water-air case, HA2O initially possesses a more aerodynamic prolate shape with a smaller frontal area, resulting in a lower initial axial acceleration (figure 8a). However, as the drop deforms into a pancake and expands radially beyond the spherical reference, its frontal area increases and its shape becomes blunter; consequently, its axial acceleration grows, and its velocity eventually exceeds that of the reference case.

A more pronounced effect is observed for HA3P and HA4O. These cases also begin with shapes that are aerodynamically favourable relative to the sphere. The lower aerodynamic forcing is accompanied with lower radial and axial deformation rates, as seen in figures 8b and 8c, where HA3P and HA4O show almost no radial expansion until $t^* \approx 0.8$. Beyond $t^* \approx 1$, these cases begin to exhibit comparable radial expansion rates as they finally approach a pancake morphology similar to the other cases. However, the initial forcing disadvantage results in a significant “lag” in both their radial lengths and centre-of-mass velocities compared to the spherical reference.

Finally, we note that the mode-frequency associated modulations in acceleration, which were prominent in the water-air system, are significantly damped here. Figure 8a shows smooth velocity profiles with minimal periodic fluctuations for the higher modes. This absence of distinct acceleration peaks at $T_{(3,0)}/4$ or $T_{(4,0)}/4$ further confirms that

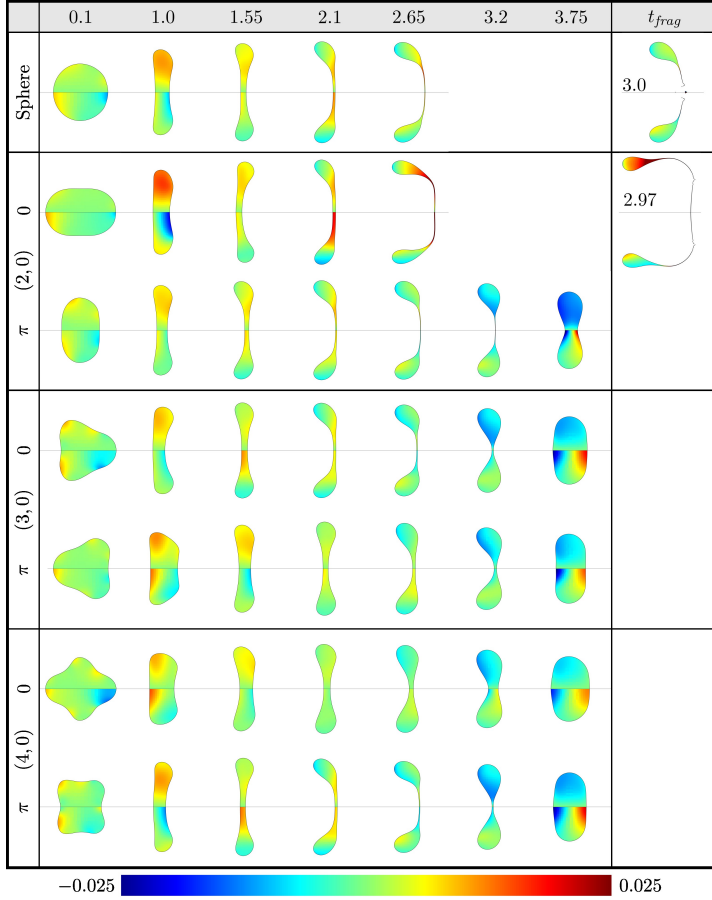


Figure 9: Temporal evolution of internal velocity fields for high-viscosity drops. The upper half of each snapshot depicts the radial velocity component, whilst the lower half displays the axial velocity component. The time sequence illustrates the enhanced viscous damping compared to the water-air system.

the influence of the initial oscillation mode on the macroscopic kinematics is far less pronounced in the high-viscosity regime, where internal damping suppresses the dynamic coupling between the drop's vibration and its trajectory.

With the exception of the more aerodynamic cases (HA3P and HA40), most cases achieve very similar radial lengths of $L_r \approx 1.6$ by $t^* \approx 1.2$, as observed in figure 8c. Generally, cases with initially less aerodynamic shapes (excluding HA20) exhibit perceptibly higher deformations and achieve thinner bags before retracting, consistent with the higher drag forces they experience during the early stages. This contrasts with the water-air system, where constructive modal coupling drove unexpectedly large deformations even for unfavourable initial shapes. The sole exception here is HA20, which exhibits higher rates of deformation and achieves or exceeds the L_r and L_z values of the spherical reference.

The internal velocity fields, presented in figure 9, reveal that the drops sustain much lower oscillatory velocities, \tilde{V} , compared to the water-air system—an expected consequence of viscous damping smoothing internal velocity gradients. Of all the cases simulated, only HA20 results in fragmentation, doing so at nearly the same time as the

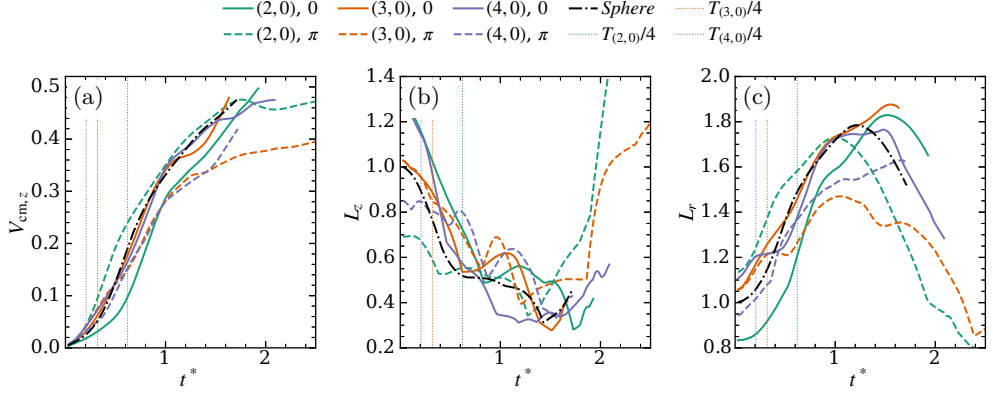


Figure 10: Temporal evolution of macroscopic kinematics for a water-like drop in a liquid ambient ($\rho = 10$). The panels display (a) the axial centre-of-mass velocity, $\mathbf{V}_{\text{cm},z}$; (b) the drop's axial length, L_z ; and (c) the radial length, L_r , as functions of dimensionless time t^* . Note the rapid acceleration of $\mathbf{V}_{\text{cm},z}$ compared to the air systems.

spherical reference case. However, the resulting bag achieves higher inflation, and the internal oscillatory velocities are significantly larger relative to the sphere.

This unique outcome for HA20 underscores the critical importance of the pressure-driven mechanism identified in the water-air system. While massive viscous dissipation suppresses the resonant modal coupling observed in the low-viscosity regime, HA20 retains the distinct physical advantage of a large pressure difference between the high-curvature upstream pole and the low-curvature periphery. This strong, geometrically induced pressure gradient is sufficient to drive radial expansion and overcome the viscous resistance, pushing the drop towards a shape topologically equivalent to HA2P. In contrast, HA2P begins with zero internal oscillatory velocity and lacks the requisite curvature-driven pressure gradient to initiate a strong internal flow. Consequently, although both phases eventually arrive at a similar geometric stage, HA2P lacks the kinetic energy required to progress to fragmentation.

For the higher modes, the role of the initial oscillation mode is largely diminished. While $\tilde{\mathbf{V}}$ peaks are still observed at regions corresponding to the subsequent geometric extremes (e.g., upstream mid-latitude regions for HA3P and HA40), the increased viscous dissipation effectively damps the feedback loop between internal flow and bulk deformation. Modal resonance, which played a major role in the water-air system, is suppressed. Instead, the initial aerodynamicity becomes the governing factor. Initially less aerodynamic drops (e.g., HA30, HA4P) capture more aerodynamic work early on and consistently show greater deformation. The (2, 0) mode remains the exception to this rule, where the non-aerodynamic π phase unexpectedly fails to match the deformation magnitude of the spherical reference, purely due to the energetic deficit described above.

In the previous sections, the drop and ambient medium possessed very large viscosity and/or density contrasts. Here, we consider the influence of the initial shape on a water-like drop impulsively accelerated in another liquid, where the density and viscosity are within an order of magnitude of the drop's properties ($\rho = 10.0$, $Oh_d = 1.258 \times 10^{-3}$, $Oh_o = 1.258 \times 10^{-3}$, $We = 10.0$). The physics of this system is governed by two coupled effects that fundamentally alter the drag dynamics compared to the air systems. First, the Ohnesorge number for the ambient phase is approximately double that of the water-air system ($Oh_{o,LL} \approx 2Oh_{o,WA}$). Since the Reynolds number scales

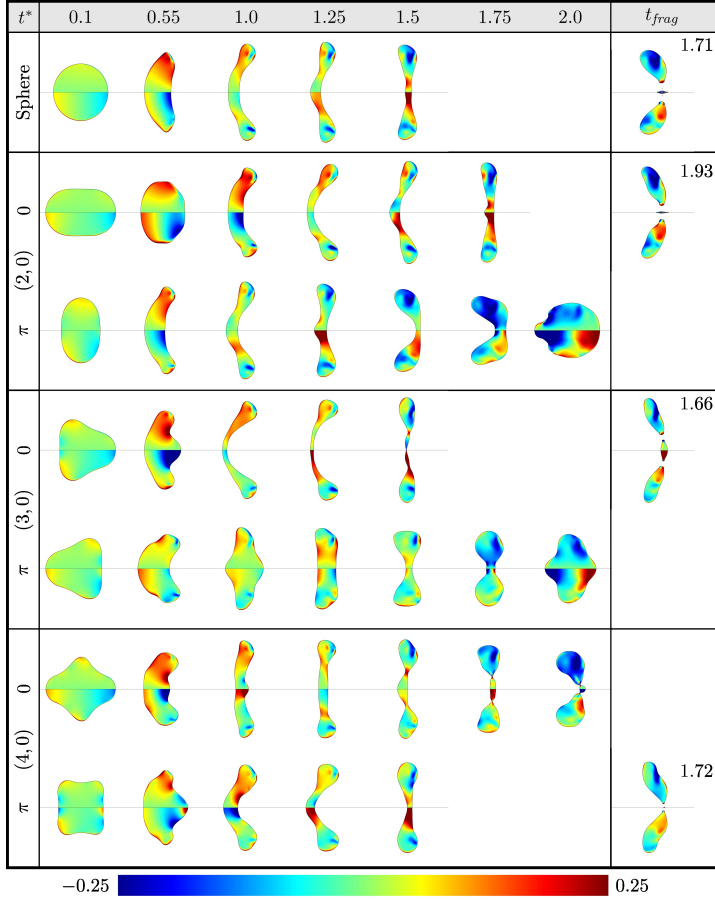


Figure 11: Temporal evolution of internal velocity fields for a water-like drop in a liquid ambient. The upper half of each snapshot depicts the radial velocity component, whilst the lower half displays the axial velocity component. The scale of $\tilde{\mathbf{V}}$ is significantly larger than in the air systems due to the lower inertia of the drop fluid.

inversely with the Ohnesorge number ($Re \propto Oh^{-1}$), the liquid-liquid system operates at an initial Reynolds number approximately half that of the air systems. Second, due to the low density ratio, the drop accelerates rapidly, significantly reducing the instantaneous relative velocity ($U_{rel} = V_{freestream} - \mathbf{V}_{cm,z}$) and thus further depressing the instantaneous Reynolds number.

The combination of lower initial Re and rapid acceleration (unsteady effects) delays the onset of flow separation. Consequently, the flow remains in the *attached viscous regime* for a much longer duration compared to the air systems. In this attached-flow regime, pressure drag (form drag) is sub-dominant, and the total drag is governed primarily by viscous skin friction. This creates an interesting inversion of the "aerodynamic" intuition established in the previous sections. Streamlined shapes (such as LL3P and LL40), which typically minimize pressure drag, allow the flow to remain attached and accelerate over their curved surfaces, generating high integrated shear stresses. In contrast, blunt shapes (like LL30) possess larger stagnation zones with lower shear. Thus, in this viscous-dominated early stage, the "more aerodynamic" shapes actually experience larger total drag forces.

This is quantitatively evident in figure 10a. Consistent with the viscous inversion hypothesis, LL3P and LL40 exhibit slightly higher initial accelerations ($d\mathbf{V}_{\text{cm},z}/dt$) than their blunt counterparts. However, it is crucial to note that these differences are markedly smaller than those observed in the air systems. With the exception of the (2, 0) mode, where a significant difference in frontal area between the prolate LL20 and oblate LL2P still controls the drag forces, the velocity profiles for the higher modes remain tightly grouped during the start of the deformation process. This prolonged similarity further supports the hypothesis that the surface areas exposed to viscous shear are comparable across these cases, and that flow separation which would drive a divergence in drag characteristics occurs much later. As the flow eventually separates, the drag mechanism transitions back to being pressure-dominated. This is observed for the (3, 0) mode, where LL3P eventually falls behind LL30 in terms of centre-of-mass velocity, indicating that the blunt LL30 ultimately generates higher drag once a wake forms. However, for the (4, 0) mode, LL40 remains at a higher centre-of-mass velocity relative to LL4P throughout the simulation window, suggesting that the initial viscous advantage gained by the 0 phase is preserved, or that its shape evolution delays the crossover to the pressure-drag regime.

Owing to the lower inertia of the drop fluid, approximately 10 times larger oscillatory velocities are observed than in the $\rho = 1000$ systems. This is evident from the $\tilde{\mathbf{V}}$ snapshots in figure 11, where radial (\tilde{V}_r) and axial (\tilde{V}_z) components as high as 0.25 units are observed.

Notable differences arise compared to the water-air system. While the fragmentation outcomes for the (2, 0) mode mirror the water-air system with only the 0 phase (LL20) achieving breakup, notable differences arise in the deformation magnitudes. Specifically, the deformation of LL2P is visibly lower compared to its water-air analog WA2P. While LL20 reaches a radial length of $L_r \approx 1.5$ at $t^* \approx 1$, LL2P achieves a similar radial length much earlier, at $t^* \approx 0.5$. This difference implies that the effective duration of impulsive acceleration for LL2P is reduced by approximately 0.5 time units. In such rapidly accelerating systems, this shortened interaction time results in a critical deficit in total energy input. This explains the significant divergence in total deformation between the two phases, a contrast not observed in the water-air system.

This energy-deficit mechanism is further exemplified by the (3, 0) mode. The more aerodynamic shape of LL3P results in lower power input during the critical initial stages. This difference in energy supply leads to a significant decrease in oscillatory velocities for LL3P relative to LL30, ultimately resulting in much lower deformation. A similar observation is made for the (4, 0) mode, where LL4P, being less aerodynamic than the spherical reference, is the only phase that captures sufficient energy to fragment.

4. Discussion

Consider a drop of diameter D , density ρ_d , viscosity μ_d , and surface tension σ subjected to impulsive acceleration. At any time t , the internal velocity field is given by $\mathbf{V}(\mathbf{x}, t)$. The volume-averaged velocity is denoted as $\mathbf{V}_{\text{cm},z}$, representing the velocity of the centre of mass. We define an *oscillatory velocity*, $\tilde{\mathbf{V}} = \mathbf{V} - \mathbf{V}_{\text{cm},z}$, which captures the internal motion of the fluid relative to the centre of mass. Consequently, the oscillatory kinetic energy associated with the drop's deformation is given by

$$\tilde{K} = \frac{1}{2} \rho_d \int_{\mathcal{V}_d} \tilde{\mathbf{V}} \cdot \tilde{\mathbf{V}} d\mathcal{V} = \tilde{K}_r + \tilde{K}_z, \quad (4.1)$$

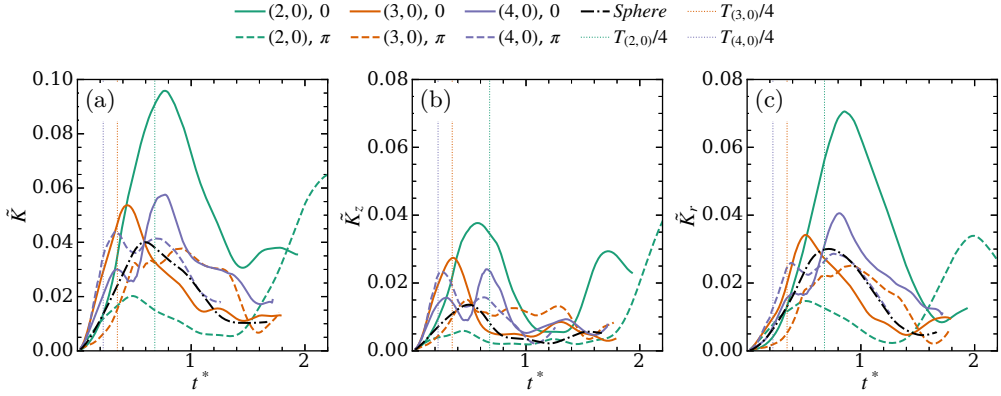


Figure 12: Temporal evolution of (a) total oscillatory kinetic energy, (b) its axial component, and (c) its radial component for a water drop in air (WAxx).

where \mathcal{V}_d is the drop volume. The total kinetic energy K decomposes into translational and oscillatory components (since the volume integral of $\mathbf{V}_{cm,z} \cdot \tilde{\mathbf{V}}$ vanishes):

$$K = K_{cm} + \tilde{K}. \quad (4.2)$$

We also evaluate the total viscous power, P_μ , by integrating the local viscous dissipation function over the drop volume:

$$P_\mu = \frac{dE_\mu}{dt} = \frac{1}{2}\mu_d \int_{\mathcal{V}_d} 2\mathbf{D} : 2\mathbf{D} \, d\mathcal{V}, \quad (4.3)$$

where $2\mathbf{D} = \nabla\mathbf{V} + (\nabla\mathbf{V})^T$ is the rate-of-deformation tensor. The cumulative energy lost to viscous dissipation up to time t is $E_\mu(t) = \int_0^t P_\mu \, dt$. The surface potential energy is defined as the excess surface energy relative to the spherical equilibrium state, $E_{pot} = \sigma(A_d - A_{sph})$, where A_d is the instantaneous surface area and $A_{sph} = \pi D^2$. Thus, by time t , the ambient medium has supplied a total energy $E = \tilde{K} + E_{pot} + K_{cm} + E_\mu$, of which $\tilde{E} = \tilde{K} + E_{pot}$ is the recoverable oscillatory energy held by the drop.

4.1. Oscillatory Kinetic Energetics

Figure 12 presents the temporal evolution of the oscillatory kinetic energy \tilde{K} , and its axial component \tilde{K}_z , and radial component \tilde{K}_r , for water drops in air (WAxx). Each peak in figure 12a represents an intermediate quasi-equilibrium state resulting from the superposition of the free modal oscillation and the forced deformation induced by the flow. From the response of the spherical reference drop, we identify a characteristic timescale for the forced deformation, $T_f \approx 0.6$, corresponding to the time required to reach the first peak in oscillatory kinetic energy. This timescale T_f can be interpreted as the quarter-period of the forced oscillation driven by the impulsive acceleration. Comparing T_f to the natural quarter-periods of the (2,0), (3,0), and (4,0) modes reveals the quality of coupling between the forced and free deformation mechanisms.

The natural quarter-period of the (2,0) mode is $T_{(2,0)}/4 \approx 0.68$, which aligns closely with T_f . For WA20, the transition from the 0 phase (prolate) to the π phase (oblate) requires internal flow from the poles to the periphery. This is kinematically compatible with the flow induced by the impulsive acceleration, which flattens the drop into a pancake. Consequently, WA20 experiences a *constructive superposition*, where the modal

and aerodynamic forces reinforce each other. Driven by this physical compatibility and precise temporal alignment ($T_{(2,0)}/4 \approx T_f$), WA20 achieves the highest \tilde{K} peak of all cases, effectively overcoming the disadvantage of its smaller, more aerodynamic frontal area. Conversely, for WA2P, the transition from π to 0 requires flow from the periphery to the poles, which directly opposes the aerodynamic forcing. This *destructive superposition* stifles the internal kinetic energy, resulting in a \tilde{K} peak almost a factor of 2 smaller than the spherical reference. Despite the larger pressure forces experienced by the aerodynamically blunt WA2P, the unfavourable modal coupling dominates, preventing fragmentation.

The (3, 0) mode introduces a timescale mismatch that fundamentally alters the coupling dynamics compared to the (2, 0) case. With a natural half-period of $T_{(3,0)}/2 \approx 0.70$, the drop nearly completes a full transition between shape extremes within the forced oscillation timescale $T_f \approx 0.6$. For WA30, the initial morphology presents a large frontal area to the free stream, generating significant pressure forces that drive fluid from the upstream pole towards the periphery. Since the transition from the 0 phase to the π phase also involves fluid movement from the upstream surface to the downstream periphery, the two flow mechanisms initially complement each other. However, the time to reach the quasi-equilibrium shape ($T_{(3,0)}/4$) is only about half the forcing timescale T_f . Consequently, as seen in figure 12a, \tilde{K} increases rapidly to reach a peak at $t^* \approx 0.50$ —approximately the midpoint between $T_{(3,0)}/4$ and T_f . Because the two contributing oscillations do not synchronize their peak energies, the maximum \tilde{K} achieved by WA30 is only modestly larger than that of the spherical reference, in stark contrast to the resonant amplification observed for WA20. Following this early peak, \tilde{K} decays even before $t^* = T_f$, mimicking the behaviour of the spherical case.

In contrast, WA3P begins with a more streamlined upstream profile, resulting in lower pressure forces driving the peripheral expansion. Furthermore, the internal flow associated with the imposed surface oscillation initially opposes the aerodynamically driven deformation. As a result, \tilde{K} grows slower than the spherical case and maintains a lower value for most of $t^* < T_f$. However, due to its short modal oscillation period, the drop transitions to the 0 configuration by $t^* \approx 0.7$, just past the forcing timescale T_f . At this stage, the drop exposes a larger frontal area to the flow while simultaneously possessing an internal velocity field that has become compatible with the external forcing. This physical configuration facilitates the transfer of external aerodynamic work into internal oscillatory kinetic energy, allowing \tilde{K} to continue growing, albeit slowly, past $t^* \approx 0.7$. A high \tilde{K} is thus sustained over a longer period, resulting in a broader, plateau-like kinetic energy profile rather than the singular, high-amplitude peak observed for WA20 and WA30. This *delayed constructive superposition* allows the π phase to recover from its initial disadvantage and achieve sufficient deformation to trigger fragmentation.

The (4, 0) mode possesses a much shorter quarter-period ($T_{(4,0)}/4 \approx 0.23$), allowing the drop to undergo a full transition to the opposite extreme and reach the next equilibrium state within the forcing timescale T_f . WA40 is initially more aerodynamic due to its axial lobes, reducing the pressure forces driving deformation. While the internal flow from the 0 to π transition is directed from the poles to the periphery (constructive), the coupling is short-lived. This is observed quantitatively in the first \tilde{K} peak at $t^* \approx 0.4$ (between $T_{(4,0)}/4$ and T_f). The magnitude of this peak is relatively small because the modal oscillation begins its restorative phase early (at $T_{(4,0)}/4$), leading to destructive superposition within the first forcing period. However, at $t^* \approx T_{(4,0)}/2$, the drop achieves a shape influenced by the π state, which experiences significantly larger aerodynamic drag. Consequently, when the drop reaches its next equilibrium state during the third

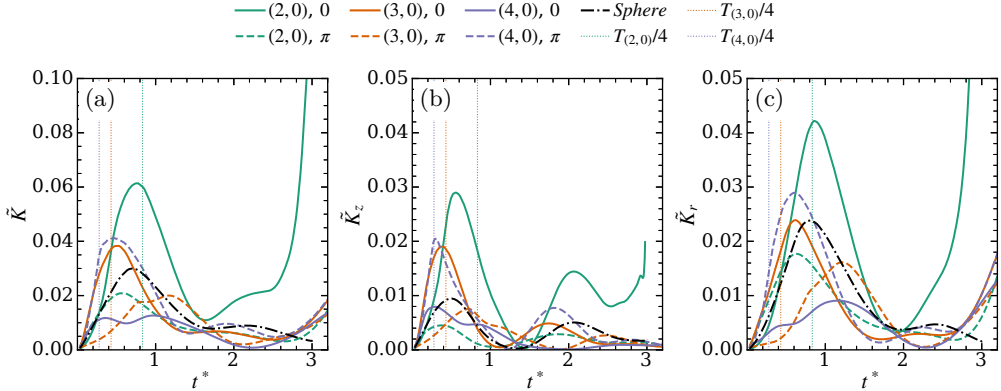


Figure 13: Total oscillatory kinetic energy, and its axial and radial components for a high viscosity drop in air are presented in figures (a), (b), and (c), respectively.

quarter-period ($t^* \approx 3T_{(4,0)}/4$), the additional aerodynamic energy results in a much larger second \tilde{K} peak as the oscillation accelerates back towards the 0 phase.

Conversely, WA4P begins with an aerodynamically unfavourable shape, experiencing large pressure forces at the onset of impulsive acceleration. The forced oscillation contributes significantly to the drop's energy, resulting in a first \tilde{K} peak that is significantly higher than that of WA40. Notably, this peak occurs at almost the same time for both cases. Thus, WA4P arrives at a similar pancake state with significantly larger kinetic energy, leading to earlier fragmentation. In fact, the fragmentation times for WA40 and WA4P differ by approximately $T_{(4,0)}/2$, suggesting that the delay in fragmentation corresponds directly to the half-period lag required for WA40 to achieve a comparable energetic state. While absolute fragmentation times from axisymmetric simulations must be treated with caution, this comparative analysis highlights a strong physical connection between the initial oscillation mode and the resulting breakup dynamics.

Let us now consider the role of initial shape on the kinetic energetics of a high-viscosity drop in air as shown in the plots in figure 13. Most of our arguments and explanations follow the description provided for the case of a water drop in air. The reference spherical case achieves its equilibrium state at $T_f \approx 0.7$, when its oscillatory kinetic energy reaches a local maximum. Apart from the reference spherical case, the only other case which fragments is HA20, which undergoes a constructive superposition with the imposed impulsive acceleration. HA20 achieves its peak \tilde{K} at $t^* \approx 0.75$, which is unsurprisingly at approximately the mid-point of T_f and $T_{(2,0)}/4 \approx 0.82$ for the high viscosity drop. Crucially, however, the prolate initial shape generates a strong pressure gradient between the pole and periphery that persists throughout the deformation. This geometric advantage allows HA20 to channel sufficient energy into radial expansion to overcome the massive viscous resistance and achieve fragmentation.

Since the drop fluid has approximately two orders of magnitude higher viscosity compared to a water drop, we expect to see much higher energy losses due to viscous dissipation and thus smaller \tilde{K} peaks. This can be inferred from figure 13a, where all cases show much smaller peaks compared to the water-air case for the same external aerodynamic forcing. The cases that deform the least — HA2P due to its strong destructive superposition, and HA3P and HA40 due to their aerodynamically favourable shapes — all exhibit peak \tilde{K} values significantly lower than the spherical reference case. The higher loss of energies also result in a larger time (and thus higher work required to be done

by aerodynamic forces) to fragmentation or to reach similar deformation levels for the higher viscosity drop.

It is also observed that the higher modes such as (3, 0) and (4, 0) only exhibit a single prominent \tilde{K} peak, since the rapid energy dissipation all but dissipates the initial oscillation mode imposed on the drop. Compared to the spherical case, any initial oscillation mode imposed on the drop apart from HA20 would increase viscous dissipation since all other initial states would either involve a strong destructive coupling right in the first half-period (in case of HA2P), or go through an entire oscillation cycle exhibiting both constructive and destructive coupling phases (in case of HA3x and HA4x). Interestingly, HA30 and HA4P cases show initial \tilde{K} peaks much larger than the spherical case, yet they fail to fragment. Similar to the case of water drops, the two cases initially have aerodynamically unfavorable shapes that experience much larger pressure forces. Much higher work is done by the external medium on the drop. For HA30, a fairly robust constructive superposition between the free and forced oscillation occurs since the flow is mostly aligned with a direction of movement away from upstream pole and towards the periphery. The appearance of a downstream axial lobe is not compliant with the formation of a pancake, which reducing the coupling efficiency. For HA4P, the flow of drop fluid towards the formation of peripheral lobes couple constructively with the aerodynamic deformation, whereas the two axial lobes do not. The higher aerodynamic work done coupled with not so great flow superposition results in peaks higher than the spherical case, but not as high as WA20. However, as the drop continues to deform past its first equilibrium state, the additional viscous dissipation incurred due to the presence of competing internal flows overcomes any initial aerodynamic advantage, \tilde{K} rapidly drops, and the drop does not fragment. Both HA3P and HA40 start with an aerodynamic disadvantage and the first peak, similar to water drop, is relatively small. While in the case of a water drop, both cases ultimately recovered their initial disadvantage, for the high viscosity drop, its higher viscous dissipation results in a small second peak and neither fragment.

In summary, the high-viscosity regime filters out the complex modal dynamics seen in water drops. Fragmentation is determined by the (2, 0) mode's unique ability to combine constructive superposition with a geometrically sustained pressure gradient that drives simple radial expansion, minimizing the viscous penalty associated with more complex shape evolutions.

In the liquid-liquid system, the ambient density and velocity match the air cases, implying similar dynamic pressure scales. However, the higher ambient viscosity ($Re \approx 0.5Re_{WA}$) maintains the flow in an attached, viscous-dominated regime. Consequently, the drop experiences significant shear stresses on its upstream surface, which actively drive fluid towards the periphery. This shear-driven mechanism sets up a faster internal flow compared to the pressure-dominated air systems, resulting in significantly higher oscillatory kinetic energies. As shown in figure 14a, peak \tilde{K} values are approximately 50% higher than those in the water-air system.

Crucially, the low density ratio means the drop has very low inertia and accelerates rapidly towards the freestream velocity. Since the aerodynamic forcing scales with the relative velocity squared ($\propto (V_{free} - \mathbf{V}_{cm,z})^2$), the available power drops precipitously with time. This creates a narrow "energy window" during the initial stages. Furthermore, it has been established that in such low-density systems where internal flow is driven by upstream shear, drops naturally deform into a forward-facing pancake (concavity pointing downstream) (Parik *et al.* 2025). Thus, any initial oscillation that kinematically

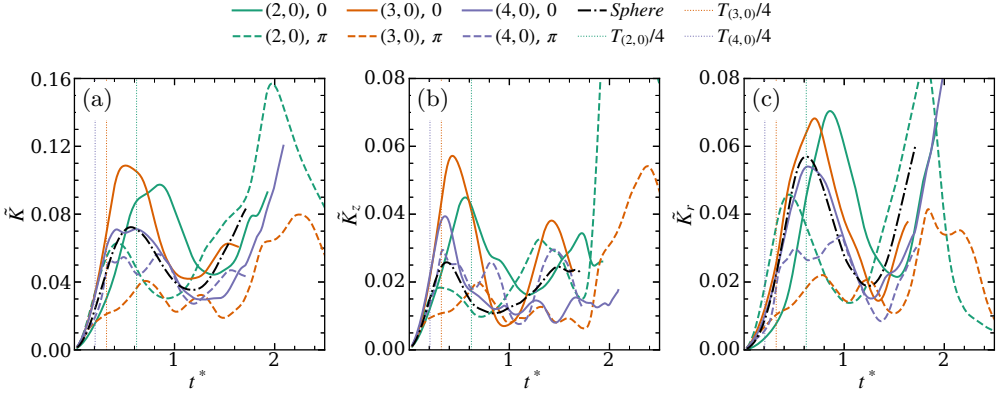


Figure 14: Total oscillatory kinetic energy, and its axial and radial components for a water drop in another liquid are presented in figures (a), (b), and (c), respectively.

supports the formation of a forward-facing pancake will constructively superpose with the impulsive deformation.

The (2, 0) mode generally follows the trends seen in the air systems. LL20 benefits from a highly efficient constructive superposition, where the transition from prolate to oblate aligns with the shear-driven flattening. Conversely, while LL2P (oblate) initially experiences larger total forcing due to its blunt profile, the internal flow required for its modal transition opposes the shear-driven deformation. This destructive superposition prevents it from capturing sufficient energy before the drop accelerates and the external forcing wanes. The efficiency of the constructive coupling for LL20 is remarkably quantitative; as seen in figure 14, the difference in peak \tilde{K} between LL20 and the spherical reference is almost exactly equal to the excess potential energy $E_{\text{pot}}(0)$ stored in the initial shape.

The (3, 0) mode offers a unique configuration for this shear-dominated regime. For LL30, the transition from the 0 to π phase involves moving fluid from the upstream surface to the downstream periphery. This internal motion closely mimics the natural shear-driven flow field required to form a forward-facing pancake. Consequently, LL30 experiences a resonance-like constructive superposition, resulting in the highest \tilde{K} peak among all simulated cases—exceeding even LL20. In contrast, LL3P begins with a streamlined shape that transitions in a way that is kinematically incompatible with the early shear forcing. By the time the drop reaches its other extreme (blunt, π -like) and becomes receptive to aerodynamic work, it has already accelerated significantly. With the relative velocity diminished, the drop cannot recover from this initial energy deficit and ultimately fails to fragment.

For LL40, the free oscillation initially aids the shear-driven deformation, redistributing fluid from axial to mid-latitude lobes to support a forward-facing pancake. This kinematic advantage leads to substantial early deformation; yet, the drop ultimately fails to fragment. The short quarter-period of the (4, 0) mode ($T_{(4,0)}/4 \approx 0.2$) implies that the drop undergoes nearly a complete oscillation cycle within the characteristic timescale of the forced deformation. Consequently, just as LL40 benefits early, it quickly transitions past this favourable quasi-equilibrium state. As the drop evolves towards a phase characterized by a bulky central core, the internal flow actively opposes the thinning required for bag formation. Once this window for efficient power input closes, the evolving configuration effectively curbs further energy capture. In contrast, LL4P successfully fragments despite starting with an incompatible kinematic state. The rapid modal oscillation enables a

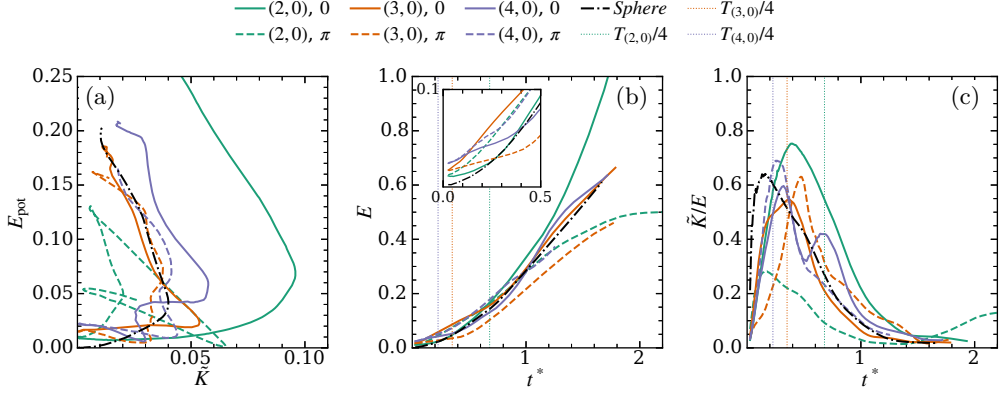


Figure 15: (a) Energy diagram plotting potential energy E_{pot} versus oscillatory kinetic energy \tilde{K} . (b) Temporal evolution of total energy supplied to the drop E . (c) Fraction of total energy converted to oscillatory kinetic energy \tilde{K}/E .

quick transition into a suitable internal flow configuration by $t^* \approx T_{(4,0)}/2$; furthermore, the subsequent retraction phase supports the evacuation of fluid from the core, facilitating bag formation and ultimate fragmentation.

4.2. Role of Initial Modes On The Fractional Energy Budget

Over the course of deformation towards fragmentation, the drops grow their surface areas by as much as a factor of 2, thus superseding any direct contribution of the initial potential energy $E_{\text{pot}}(0)$ in the peak oscillatory kinetic energies gained by the drops. This is evident from the energy diagram in the plot of potential energy against the oscillatory kinetic energy for a water drop in air as shown in figure 15a. E_{pot} grows by as much as an order of magnitude and $E_{\text{pot}}(0)$ is much smaller than the increase in peak \tilde{K} relative to the spherical case, showing that the initially supplied additional surface energy $E_{\text{pot}}(0)$ cannot solely account for the additional \tilde{K} in the 0 phase. From the energy diagram, we also note that except for the case that does not fragment, all other cases show almost constant or even a decrease in E_{pot} and a simultaneous growth in \tilde{K} during the deformation towards the quasi-equilibrium shape. This hints at a preferential transfer of work done by the freestream towards amplifying oscillatory energy in the drop (instead of E_{pot} for instance). In fact, the primary mechanism through which an initial shape affects the energetics of the drop over the course of its deformation is by modulating the distribution of total work performed by the aerodynamic forces on the drop (E). The coupling between the initial mode and the impulsive acceleration determines how this external work is partitioned between translational kinetic energy (K_{cm}), oscillatory energy ($\tilde{K} + E_{\text{pot}}$), and viscous dissipation (E_{μ}).

The total energy captured by the drop is shown in figure 15b. During the initial stages ($t^* < 0.5$), cases with less aerodynamic shapes, specifically WA2P, WA30, and WA4P, capture energy most rapidly, as their large, blunt frontal areas allow pressure forces to perform significant work. Conversely, WA3P, with its streamlined initial profile, captures significantly less energy until $t^* \approx 0.4$, resulting in a net energy deficit of approximately 15% compared to the other cases by $t^* \approx 1$. However, for most cases, the differences in total energy supply (E) are relatively small. Thus, the drastic differences in fragmentation

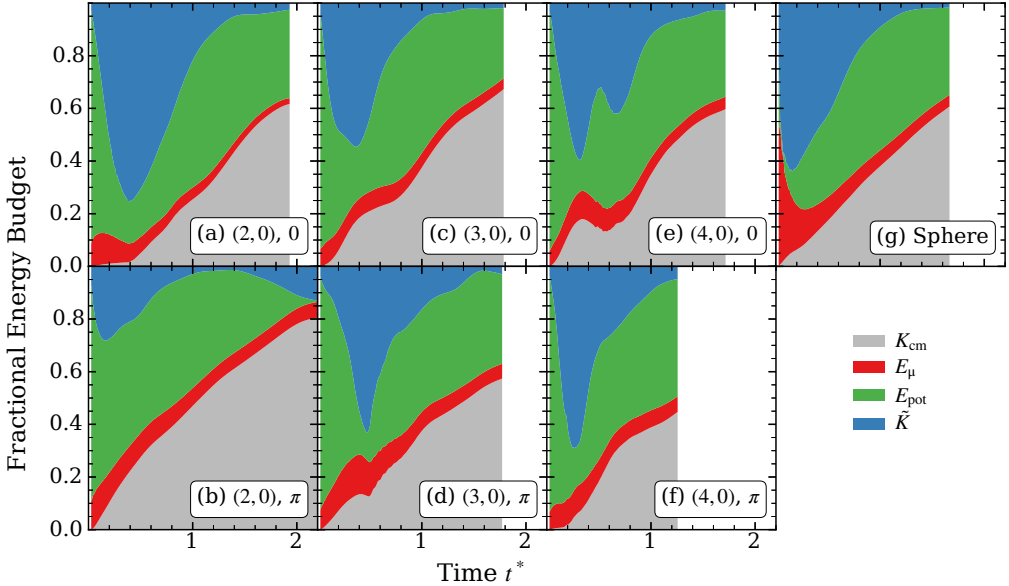


Figure 16: Temporal evolution of the fractional energy budget for a water drop in air. The total energy is decomposed into translational kinetic energy (K_{cm}), viscous dissipation (E_{μ}), additional surface energy (E_{pot}), and oscillatory kinetic energy (\tilde{K}), all normalized by the instantaneous total energy supplied to the drop E .

outcome are driven primarily by the efficiency of energy partitioning rather than the total magnitude of energy capture.

Figure 16 visualizes this partitioning by plotting the various energy components as fractions of the instantaneous total energy E . Panel (a) clearly illustrates why WA20 achieves the highest oscillatory kinetic energies. For $t^* < 0.4$, WA20 channels almost all input energy into deformation (\tilde{K}) and viscous dissipation (E_{μ}), with negligible transfer to centre-of-mass acceleration. This explains the "slow start" in $\mathbf{V}_{\text{cm},z}$ observed in the Results section: the aerodynamic work is being utilized to deform the drop radially rather than accelerate it axially. Consequently, WA20 holds nearly 80% of its total energy in the oscillatory mode at its peak.

In contrast, WA2P preferentially transfers energy to translational motion. By $t^* \approx T_f$, nearly 40% of its total energy is locked in K_{cm} , compared to less than 20% for the other cases. This leaves a significantly reduced fraction (only $\approx 20\%$) available for oscillatory kinetic energy. Despite the larger total forces acting on the blunt WA2P drop, this inefficient partitioning stifles the deformation. Notably, the peak energy fraction for WA2P occurs very early ($t^* \approx 0.15$), mimicking the spherical reference, whereas the resonant WA20 case sustains its energy growth until $t^* \geq 0.4$.

Finally, the role of viscous dissipation (E_{μ}), represented by the red region, reveals a non-conservative energetic cost of deformation. While the cumulative dissipation is comparable across cases, the fractional rate of dissipation increases distinctly during periods of rapid \tilde{K} growth (e.g., for WA40). This is expected, as establishing the strong internal velocity gradients required for oscillation inherently generates higher shear rates. Thus, successful fragmentation requires a mode that not only captures aerodynamic energy but channels it into \tilde{K} efficiently enough to overcome this viscous cost.

For the high-viscosity drop, the energy supply shown in figure 17b follows a similar

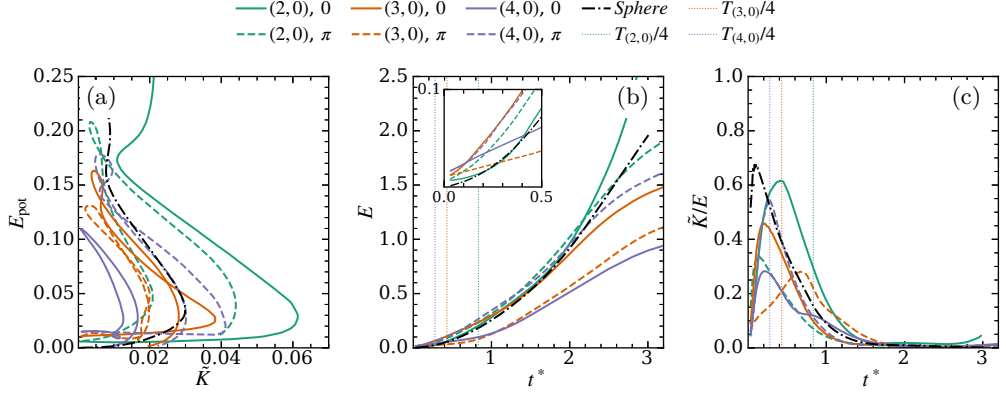


Figure 17: (a) Energy diagram plotting potential energy E_{pot} versus oscillatory kinetic energy \tilde{K} . (b) Temporal evolution of total energy supplied to the drop E . (c) Fraction of total energy converted to oscillatory kinetic energy \tilde{K}/E .

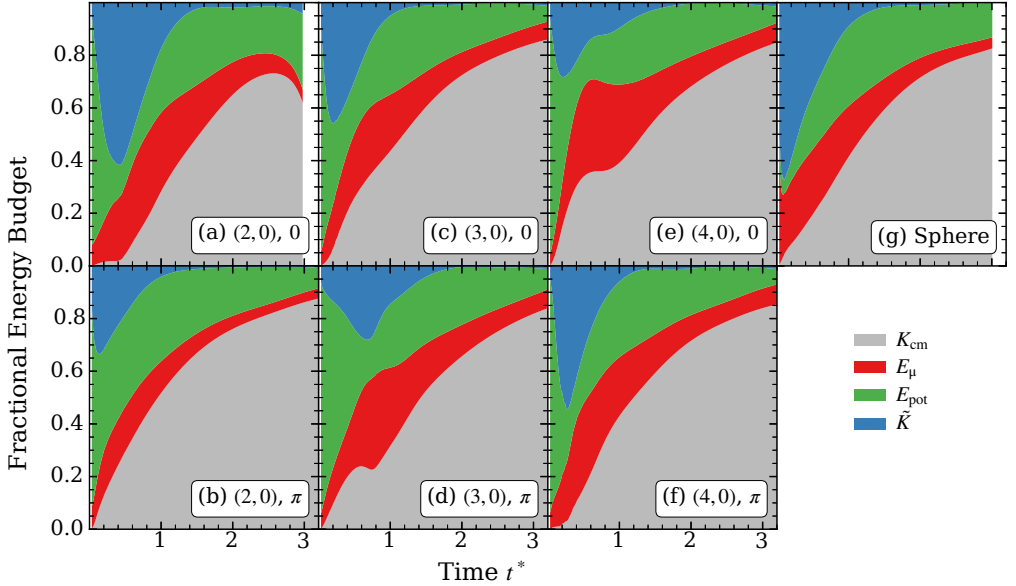


Figure 18: Temporal evolution of the fractional energy budget for a high-viscosity drop in air. The total energy is decomposed into translational kinetic energy (K_{cm}), viscous dissipation (E_{μ}), additional surface energy (E_{pot}), and oscillatory kinetic energy (\tilde{K}), all normalized by the instantaneous total energy supplied to the drop E .

trend to the water-air system, with all cases capturing comparable amounts of total energy during the initial deformation phase. However, the partitioning of this energy is fundamentally altered by the viscous stress. As evident in figure 18, the viscous dissipation fraction (E_{μ} , red region) is substantial for all cases, representing a significant negative power flow on any internal motion.

Despite the significant energy losses, the fragmentation outcome ultimately is determined by how the remaining energy is allocated. HA20 mimics the efficient partitioning

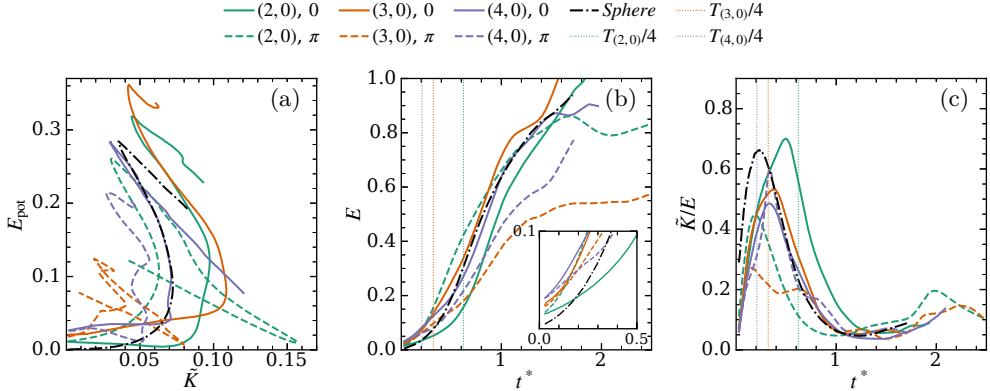


Figure 19: Energy diagrams for a water drop impulsively accelerated in a similar liquid.

of the spherical reference, channeling nearly 60% of its total energy into the oscillatory mode ($\tilde{K} + E_{\text{pot}}$). Crucially, it maintains a relatively low fraction of translational energy (K_{cm}). In contrast, HA2P mirrors the behaviour of its low-viscosity counterpart (WA2P), locking a large fraction of input energy into accelerating the centre of mass (K_{cm}) rather than deforming the drop. Due to the absence of strong internal oscillatory velocities, HA2P actually incurs lower viscous dissipation than HA20, yet it fails to fragment because the energy is essentially "wasted" on translation.

The cases HA30 and HA4P present an interesting nuance. Recall from figure 17a that these cases achieve remarkably high absolute \tilde{K} peaks, higher than the fragmenting sphere. However, the fractional budget reveals why this energy is insufficient for breakup. Neither case reaches the 60% oscillatory fraction threshold seen in HA20. Furthermore, both cases exhibit a rapid expansion of the E_{μ} region immediately following their peak \tilde{K} . This indicates that the complex internal flows associated with these modes (e.g., competing lobed structures) generate severe velocity gradients that incur a higher viscous penalty than the simple radial expansion of HA20. Thus, high viscosity selectively dampens these complex modes, dissipating their energy before it can drive the drop to the fragmentation limit.

In case of a water drop impulsively accelerated in another liquid, the problem is strongly controlled by the low density ratio of the system. The drop has two orders of magnitude less inertia, which results in it gaining much higher center-of-mass velocities (approximately 50% of the freestream) by the end of fragmentation process. As a result, the power input wanes in the later stages of the process. Thus, the quality of coupling between the initial modes and the forced oscillation, as well as the amount of aerodynamic forcing acting on the drop during the first two quarter periods play the biggest role in controlling the total conserved energy held by the oscillation. A tool to understand this is through the fractional energy budget plots for all the seven cases, including the reference spherical case, which informs us of the fragmentation threshold energy distribution. This is shown in figure 20.

The cases that fragment, i.e., LL20, LL30, and LL4P, are distinguished by their ability to channel a larger fraction of early work into \tilde{K} . All three maintain higher total oscillatory energies ($\tilde{K} + E_{\text{pot}}$) than the spherical reference throughout the deformation. The budget for LL40 offers a final confirmation of the hypothesis proposed earlier. During the first quarter-period, LL40 actually partitions a higher fraction of energy into \tilde{K} than LL4P, benefiting from its favourable initial coupling. However, as it transitions past this

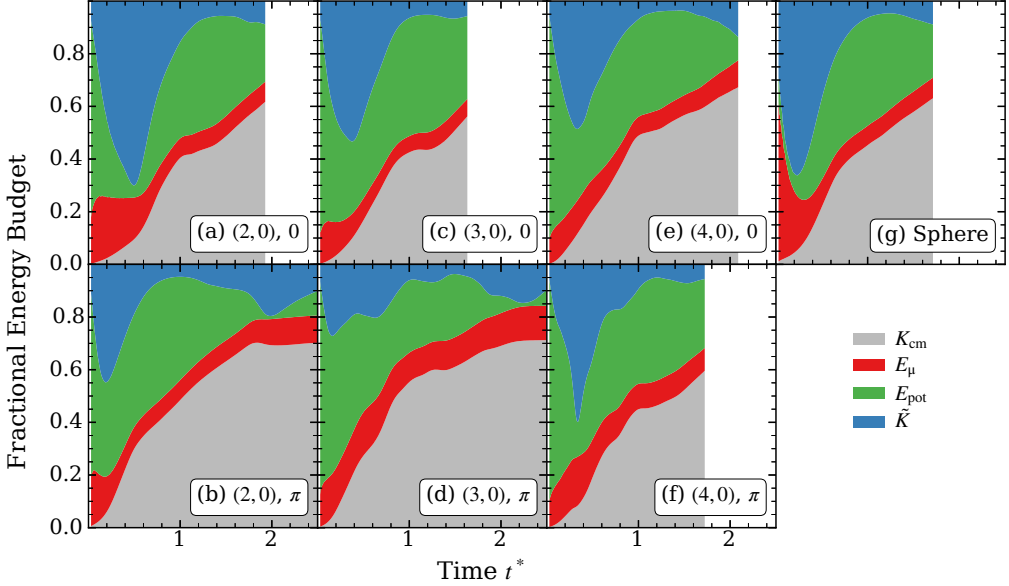


Figure 20: Temporal evolution of the fractional energy budget for a water drop in a liquid ambient. The total energy is decomposed into translational kinetic energy (K_{cm}), viscous dissipation (E_μ), additional surface energy (E_{pot}), and oscillatory kinetic energy (\tilde{K}), all normalized by the instantaneous total energy supplied to the drop E .

optimal state, the coupling degrades. This manifests in a smaller fraction of total energy being partitioned for \tilde{K} at its peak, resulting in relatively less deformation for LL40. In contrast, LL4P starts with a lower oscillatory fraction but rapidly improves its partitioning efficiency. Because LL4P achieves its peak efficiency while the relative velocity is still sufficiently high, it secures the net energy required for fragmentation, whereas the early advantage of LL40 is insufficient to sustain the deformation once the external forcing wanes. However, we note that there are small differences in the coupling quality between the two phases and the amount of deformation is fairly similar.

5. Conclusions

In this study, we systematically investigated how the initial shape of a drop affects its deformation and breakup under impulsive acceleration. Using the framework of axisymmetric Rayleigh modes, we analyzed three distinct physical systems: a water drop in air, a high-viscosity drop in air, and a water drop in another liquid. The key conclusions from this work are summarized below:

- **Dynamic Coupling Dominates Static Aerodynamics:** The fate of a drop is not determined merely by its initial drag coefficient. Instead, it is governed by the dynamic coupling between the drop's internal flow and the external aerodynamic forcing. When the internal flow of the initial mode aligns with the forced deformation (constructive superposition), the drop captures more energy and is more likely to fragment. Conversely, if the internal flow opposes the forcing (destructive superposition), the drop stabilizes.

- **Resonance and Timing in Water-Air Systems:** A characteristic forcing timescale, $T_f \approx 0.6$, associated with the impulsive aerodynamic deformation can be identified. The fundamental (2,0) mode possesses a natural quarter-period

$(T_{(2,0)}/4 \approx 0.68)$ that aligns closely with this forcing timescale. For the prolate (0) phase, this temporal synchronization combines with a kinematically compatible internal flow (pole-to-periphery) to drive a resonant coupling, ensuring fragmentation. For higher modes, the outcome depends on how their oscillation periods synchronize with T_f . A "recovery mechanism" was observed where initially unfavorable shapes (like the π phase of the (4, 0) mode) transition into a favorable configuration exactly when the aerodynamic forcing is strongest, whereas favorable shapes often transition out too quickly.

- **Viscous Dissipation is Paramount in High-Viscosity Drops:** In the high-viscosity regime, internal viscous dissipation becomes the primary barrier to fragmentation, overriding the modal resonance effects seen in water drops. Higher modes ($n = 3, 4$) involve complex internal flow structures (e.g., competing lobes) that generate high shear rates and thus result in excessive viscous dissipation. This increased energy loss is only overcome for equally large aerodynamic and coupling advantages, the only such case being HA20 case. While the aerodynamic shapes experience lower drag, they fundamentally lack the necessary aerodynamic power input to offset the increased viscous losses and thus show visibly less deformation.

- **Shear-Driven Deformation in Liquid-Liquid Systems:** Liquid-liquid systems are characterized by low density ratios, and thus droplet drop accelerates rapidly, and the flow remains attached to a larger proportion of the fragmentation process. In this regime, shear stresses on the upstream face drive the deformation, favouring the formation of a "forward-facing pancake." Initial modes that kinematically support this specific shape (like the (3, 0) mode) capture massive amounts of oscillatory energy. However, because the drop accelerates so fast, the relative velocity decays quickly. This creates a small time window of efficient power input. Drops that cannot capture energy early enough or those that transition out of a favourable state too quickly fail to fragment.

- **Energy Partitioning as the Threshold:** Across all systems, the total energy supplied to the drop is often comparable. The determining factor for breakup is the efficiency of energy partitioning. Successful fragmentation occurs only when the drop channels a high fraction of the external work into oscillatory kinetic energy (\tilde{K}). Cases that fail to fragment typically "waste" the energy by converting it into bulk translation (K_{cm}) or losing it to viscous dissipation (E_μ).

In summary, the initial Rayleigh mode acts as a dynamic initial condition that sets the trajectory of the drop through the energy landscape. Predicting secondary fragmentation requires accounting for this initial phase, as it can shift the outcome from catastrophic breakup to stability.

6. Acknowledgment

We wish to acknowledge the support of TACC for the compute time on Frontera under the Pathways program, which allowed us to conduct these computationally intensive simulations. We would also like to thank for the compute time on Utah CHPC.

Appendix A. Derivation of the Volume-Correction Factor b_0

This appendix details the derivation of the volume-conserving equation for the corrected base radius, b_0 , presented in the main text in equation 2.2.

We aim to obtain a general form of b_0 for the superposition of any arbitrary number of Rayleigh modes and amplitudes. We do this by assuming that the volume of the drop is a constant for any and all superposed perturbations.

$$\frac{4}{3}\pi R_0^3 = 2\pi \int_{\theta=0}^{\pi} \int_{r=0}^{r_n(\theta)} r_n^2 dr \sin \theta d\theta \quad (\text{A } 1)$$

$$= \frac{2\pi}{3} \int_{\theta=0}^{\pi} [r_n(\theta)]^3 \sin \theta d\theta \quad (\text{A } 2)$$

$$2R_0^3 = \int_{\theta=0}^{\pi} \left[b_0 + \sum_{n=2}^{n \rightarrow \infty} A_n P_n(\cos \theta) \right]^3 \sin \theta d\theta \quad (\text{A } 3a)$$

$$= b_0^3 \int_{\theta=0}^{\pi} \left[1 + \frac{3}{b_0} \left(\sum_{n=2}^{n \rightarrow \infty} A_n P_n(\cos \theta) \right) \right. \quad (\text{A } 3b)$$

$$\left. + \frac{3}{b_0^2} \left(\sum_{n=2}^{n \rightarrow \infty} A_n P_n(\cos \theta) \right)^2 \right] \sin \theta d\theta \quad (\text{A } 3c)$$

$$\left. + \frac{1}{b_0^2} \left(\sum_{n=2}^{n \rightarrow \infty} A_n P_n(\cos \theta) \right)^3 \right] \sin \theta d\theta \quad (\text{A } 3d)$$

$$2R_0^3 = b_0^3 \int_{\theta=0}^{\pi} \left[\sin \theta d\theta + \frac{3}{b_0} \left(\sum_{n=2}^{n \rightarrow \infty} A_n P_n(\cos \theta) \right) \sin \theta d\theta \right. \quad (\text{A } 4a)$$

$$\left. + \frac{3}{b_0^2} \left(\sum_{n=2}^{n \rightarrow \infty} A_n P_n(\cos \theta) \right)^2 \sin \theta d\theta \right] \sin \theta d\theta \quad (\text{A } 4b)$$

$$\left. + \frac{1}{b_0^2} \left(\sum_{n=2}^{n \rightarrow \infty} A_n P_n(\cos \theta) \right)^3 \sin \theta d\theta \right] \sin \theta d\theta \quad (\text{A } 4c)$$

The Legendre polynomials are orthogonal, which implies that the integrals of the product of two different Legendre polynomials over the interval $[-1, 1]$ is zero, given that the polynomials are of different orders.

$$\int_{-1}^1 P_n(x) P_m(x) dx = \int_0^{\pi} P_n(\cos \theta) P_m(\cos \theta) \sin \theta d\theta = 0 \quad \text{for } n \neq m \quad (\text{A } 5)$$

Setting $m = 0$ in equation A 5 ($P_0(x) = 1$), we get:

$$\int_0^{\pi} P_n(\cos \theta) \sin \theta d\theta = 0 \quad \text{for } 2 \leq n < \infty \quad (\text{A } 6)$$

We can also evaluate each of the integrals in equation A 4 as follows:

$$\int_0^{\pi} \sin \theta d\theta = 2 \quad (\text{A } 7)$$

$$\frac{3}{b_0^2} \left(\sum_{n=2}^{n \rightarrow \infty} A_n P_n(\cos \theta) \right)^2 \sin \theta d\theta = \frac{6}{b_0^2} \sum_{n=2}^{n \rightarrow \infty} \frac{A_n^2}{2n+1} \quad (\text{A } 8)$$

$$\frac{1}{b_0^3} \left(\sum_{n=2}^{n \rightarrow \infty} A_n P_n(\cos \theta) \right)^3 \sin \theta \, d\theta = \frac{2}{b_0^3} \sum_{i,j,k}^{\infty} A_i A_j A_k \begin{pmatrix} i & j & k \\ 0 & 0 & 0 \end{pmatrix}^2 \quad (\text{A 9})$$

Here, $\begin{pmatrix} i & j & k \\ 0 & 0 & 0 \end{pmatrix}$ is a specific case of the general Wigner 3-j symbol and evaluates to a scalar. For $s = 0.5(i + j + k)$, the Wigner 3-j symbol is given by:

$$\begin{pmatrix} i & j & k \\ 0 & 0 & 0 \end{pmatrix} = (-1)^s \left[\frac{s!}{(s-i)!(s-j)!(s-k)!} \right] \sqrt{\frac{[2(s-i)]! [2(s-j)]! [2(s-k)]!}{[2s+1]!}} \quad (\text{A 10})$$

Substituting equations A 7, A 8, and A 9 into equation A 4 and simplifying gives us:

$$2R_0^3 = b_0^3 \left[2 + \frac{6}{b_0^2} \sum_{n=2}^{n \rightarrow \infty} \frac{A_n^2}{2n+1} + \frac{2}{b_0^3} \sum_{i,j,k}^{\infty} A_i A_j A_k \begin{pmatrix} i & j & k \\ 0 & 0 & 0 \end{pmatrix}^2 \right] \quad (\text{A 11})$$

Non-dimensionalizing all length scales in equation A 11 by the drop diameter $2R_0$ and setting $b_0 = \tilde{b}_0 D$ and $A_n = \tilde{A}_n D$ gives us:

$$1 = 8\tilde{b}_0^3 + 24\tilde{b}_0 \sum_{n=2}^{n \rightarrow \infty} \frac{\tilde{A}_n^2}{2n+1} + 8 \sum_{i,j,k}^{\infty} \tilde{A}_i \tilde{A}_j \tilde{A}_k \begin{pmatrix} i & j & k \\ 0 & 0 & 0 \end{pmatrix}^2 \quad (\text{A 12})$$

Equation A 12 is a cubic equation in \tilde{b}_0 which can be solved using any standard numerical root-finding algorithm. Since this is a one-time calculation, the computational cost of solving this equation is negligible. We know that \tilde{b}_0 is bounded between 0 and 0.5 (for infinitesimal perturbations), and hence the solution to equation A 12 is guaranteed using the bisection method.

Appendix B. Experimental Setup

The experiments were conducted in the Splash Lab at King Abdullah University of Science and Technology (KAUST) using a custom-built air jet facility designed to investigate the aerodynamic breakup of large liquid droplets. A schematic representation of the experimental setup is shown in Figure 21. The setup comprises several key components: a novel droplet formation and release mechanism, an air jet system with a conical outlet, a movable plate assembly for impulsive exposure of the droplet to the air stream, and a solenoid-based triggering system. The design and operation of the large droplet generation and release mechanism are described in detail in previous studies Fonnebeek (2022); Dighe *et al.* (2024). In each experiment, a single droplet is formed and released such that it falls vertically under the influence of gravity, undergoing natural (2, 0) mode shape oscillations during free fall. The air jet used to induce aerodynamic breakup is generated by an AC Infinity fan (Model AL-CLT8) equipped with a custom-designed conical outlet. A honeycomb structure positioned inside the cone serves to straighten the flow and reduce turbulence intensity. The air jet velocity is measured using a hot-wire anemometer (Dantec MiniCTA 54T42), ensuring accurate characterization of the airflow.

During the free fall of the droplet, the air jet is initially obstructed by a square sliding plate mounted on the inner guides of an aluminum frame. The plate is held in a locked position above the air jet by rubber bands, maintaining tension until release. Once the droplet reaches the desired height and deformation state, the plate is rapidly retracted by actuating a solenoid, thereby exposing the droplet impulsively to the air jet. The subsequent breakup process is recorded using high-speed shadowgraphy with

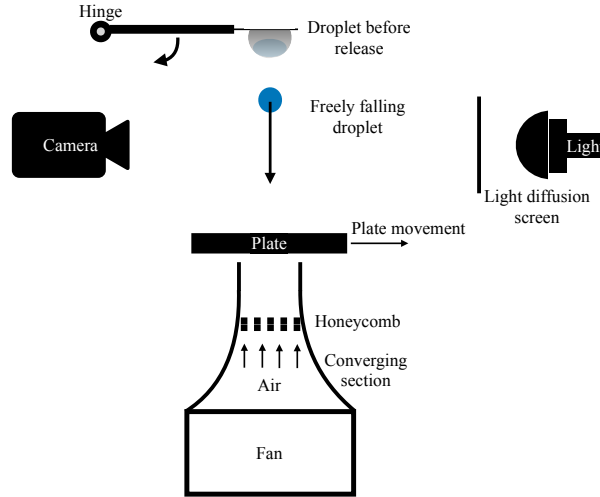


Figure 21: Overview of the experimental setup designed to study the aerodynamic breakup of large droplets. The setup includes a custom droplet generation and release mechanism, a fan with a conical outlet and honeycomb flow straightener for air-jet formation, a sliding plate for impulsive exposure of the droplet to the jet, and the setup of the high-speed shadowgraphy system for visualization.

a Phantom TMX-6410 camera operating at 10,000 frames per second. This imaging technique provides high temporal and spatial resolution necessary to capture the transient dynamics of droplet deformation and breakup.

Appendix C. Test of Convergence of Higher Order Derived Metrics

As has been discussed in section 3 and 4, higher order properties such as kinetic energy, surface energy, and viscous dissipation are essential metrics obtained from the simulations. However, the convergence of first order statistics such as velocity field and volume fraction field does not ensure that second order statistics are also converged with respect to the grid resolution. In order to test the convergence of these second order metrics, we simulate the impulsive acceleration of a water drop in air ($\rho \approx 816$, $Oho \approx 0.0007$, $Ohd = 0.0013$, and $We_0 = 12$) for 3 different maximum refinement levels and 4 different wavelet error thresholds for the velocity field. Figure 22 illustrates all the convergence plots in the first row, i.e., panels (a), (b), and (c), and the corresponding relative errors with respect to the simulation with $N = 14$, $\chi_u = 10^{-5}$ (i.e., highest resolutions are strictest error thresholds tested). For all metrics, the relative error remains below 10^{-2} for the parameters of choice for this work, i.e., $N = 14$ and $\chi_u = 10^{-4}$ confirming the convergence of energy and dissipation metrics obtained from the simulations.

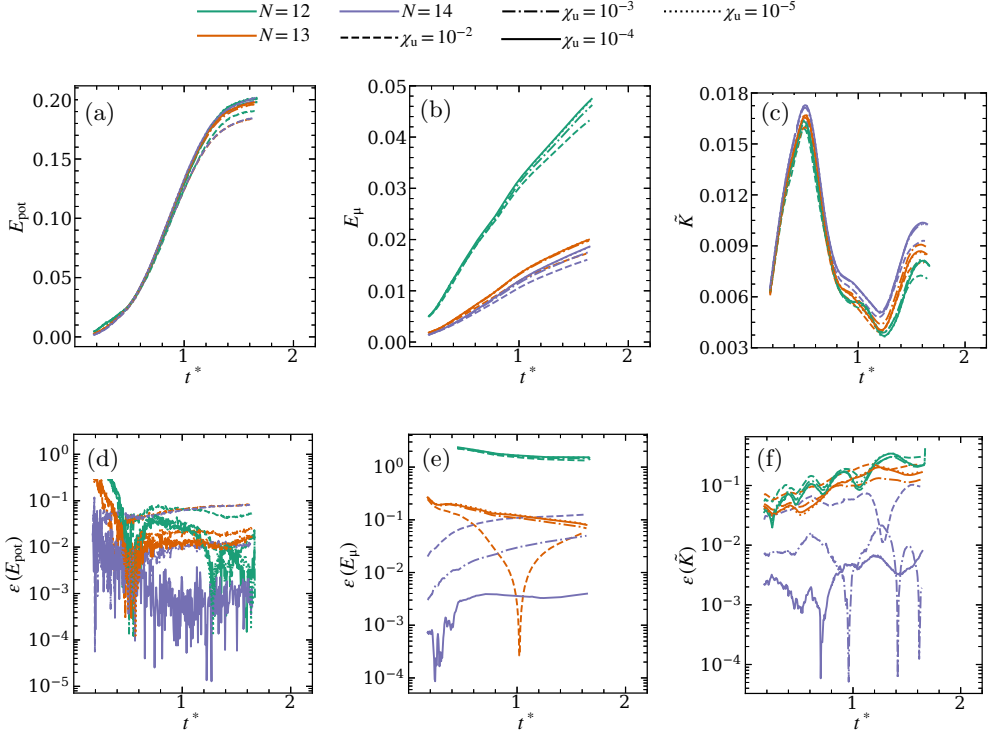


Figure 22: Temporal development of additional Surface Energy (E_{pot}), cumulative viscous dissipation (E_{μ}), and oscillatory kinetic energy (\tilde{K}) are plotted for different values of maximum allowed refinement level N (minimum allowed cell size), and wavelet error threshold for the velocity field χ_u are shown in panels (a), (b), and (c), respectively. Panels (d), (e), and (f) show the corresponding relative errors with respect to the best guess corresponding to $N = 14$, $\chi = 10^{-5}$. All three metrics converge for the parameters $N = 14$, $\chi = 10^{-4}$, as seen from their relative errors which remain below 10^{-2} for the entire duration.

REFERENCES

AGRAWAL, MEENU, KATIYAR, RAJAT KUMAR, KARRI, BADARINATH & SAHU, KIRTI CHANDRA 2020 Experimental investigation of a nonspherical water droplet falling in air. *Physics of Fluids* **32** (11), 112105.

AGRAWAL, MEENU, PREMLATA, A. R., TRIPATHI, MANOJ KUMAR, KARRI, BADARINATH & SAHU, KIRTI CHANDRA 2017 Nonspherical liquid droplet falling in air. *Physical Review E* **95** (3), 033111.

BALLA, MOUNIKA, KUMAR TRIPATHI, MANOJ & SAHU, KIRTI CHANDRA 2019 Shape oscillations of a nonspherical water droplet. *Physical Review E* **99** (2), 023107.

BASARAN, OSMAN A. 1992 Nonlinear oscillations of viscous liquid drops. *Journal of Fluid Mechanics* **241**, 169–198.

BECKER, E., HILLER, W. J. & KOWALEWSKI, T. A. 1991 Experimental and theoretical investigation of large-amplitude oscillations of liquid droplets. *Journal of Fluid Mechanics* **231**, 189–210.

BECKER, E., HILLER, W. J. & KOWALEWSKI, T. A. 1994 Nonlinear dynamics of viscous droplets. *Journal of Fluid Mechanics* **258**, 191–216.

BRACKBILL, J. U., KOTHE, D. B & ZEMACH, C 1992 A continuum method for modeling surface tension. *Journal of Computational Physics* **100** (2), 335–354.

BRANT FOOTE, G 1973 A numerical method for studying liquid drop behavior: Simple oscillation. *Journal of Computational Physics* **11** (4), 507–530.

CHANDRASEKHAR, S. 1959 The Oscillations of a Viscous Liquid Globe. *Proceedings of the London Mathematical Society* **s3-9** (1), 141–149.

DIGHE, SANDIP, MAITY, DILIP KUMAR, FONNESBECK, JEFFREY N., DUTTA, SOM & TRUSCOTT, TADD 2024 Extremely large water droplet impact onto a deep liquid pool. *Physical Review E* **109** (4), 045107.

FARSOIYA, PALAS KUMAR, POPINET, STÉPHANE & DEIKE, LUC 2021 Bubble-mediated transfer of dilute gas in turbulence. *Journal of Fluid Mechanics* **920**, A34.

FLOCK, A.K., GUILDENBECHER, D.R., CHEN, J., SOJKA, P.E. & BAUER, H.-J. 2012 Experimental statistics of droplet trajectory and air flow during aerodynamic fragmentation of liquid drops. *International Journal of Multiphase Flow* **47**, 37–49.

FONNESBECK, JEFFREY 2022 Release of Large Water Droplets. Master's thesis, Utah State University, Logan, UT.

FRANCOIS, MARIANNE M., CUMMINS, SHAREN J., DENDY, EDWARD D., KOTHE, DOUGLAS B., SICILIAN, JAMES M. & WILLIAMS, MATTHEW W. 2006 A balanced-force algorithm for continuous and sharp interfacial surface tension models within a volume tracking framework. *Journal of Computational Physics* **213** (1), 141–173.

HINZE, J. O. 1955 Fundamentals of the hydrodynamic mechanism of splitting in dispersion processes. *AIChE Journal* **1** (3), 289–295.

HSIANG, LP & FAETH, GM 1995 Drop deformation and breakup due to shock wave and steady disturbances. *International Journal of Multiphase Flow* **21** (4), 545–560.

JACKIW, ISAAC M. & ASHGRIZ, NASSER 2021 On aerodynamic droplet breakup. *Journal of Fluid Mechanics* **913** (A33), 1–46.

KULKARNI, V. & SOJKA, P. E. 2014 Bag breakup of low viscosity drops in the presence of a continuous air jet. *Physics of Fluids* **26** (7), 072103.

LAMB, SIR HORACE 1932 *Hydrodynamics*, 6th edn. Cambridge: Cambridge University Press.

MERADJI, S., LYUBIMOVA, T.P., LYUBIMOV, D.V. & ROUX, B. 2001 Numerical Simulation of a Liquid Drop Freely Oscillating. *Crystal Research and Technology* **36** (7), 729–744.

PARIK, ADITYA, TRUSCOTT, TADD T. & DUTTA, SOM 2025 On the threshold of drop fragmentation under impulsive acceleration. *Journal of Fluid Mechanics* **1019**, A1.

POPINET, STÉPHANE 2003 Gerris: A tree-based adaptive solver for the incompressible Euler equations in complex geometries. *Journal of Computational Physics* **190** (2), 572–600.

POPINET, STÉPHANE 2009 An accurate adaptive solver for surface-tension-driven interfacial flows. *Journal of Computational Physics* **228** (16), 5838–5866.

POPINET, STÉPHANE 2015 A quadtree-adaptive multigrid solver for the Serre–Green–Naghdi equations. *Journal of Computational Physics* **302**, 336–358.

POPINET, STEPHANE & ZALESKI, STÉPHANE 1999 A front-tracking algorithm for accurate

representation of surface tension. *International Journal for Numerical Methods in Fluids* **30** (6), 775–793.

RAYLEIGH, LORD 1879 VI. On the capillary phenomena of jets. *Proceedings of the Royal Society of London* **29** (196-199), 71–97.

SZAKÁLL, MIKLOÓS, DIEHL, KAROLINE & MITRA, SUBIR K. 2009 A wind tunnel study on the shape, oscillation, and internal circulation of large raindrops with sizes between 2.5 and 7.5 mm. *Journal of the Atmospheric Sciences* **66** (3), 755–765.

SZAKÁLL, MIKLÓS, MITRA, SUBIR K., DIEHL, KAROLINE & BORRMANN, STEPHAN 2010 Shapes and oscillations of falling raindrops — A review. *Atmospheric Research* **97** (4), 416–425.

TRINH, E. & WANG, T. G. 1982 Large-amplitude free and driven drop-shape oscillations: Experimental observations. *Journal of Fluid Mechanics* **122**, 315–338.

TSAMOPOULOS, JOHN A. & BROWN, ROBERT A. 1983 Nonlinear oscillations of inviscid drops and bubbles. *Journal of Fluid Mechanics* **127**, 519–537.

VAN HOOFT, J. ANTOON, POPINET, STÉPHANE, VAN HEERWAARDEN, CHIEL C., VAN DER LINDEN, STEVEN J. A., DE ROODE, STEPHAN R. & VAN DE WIEL, BAS J. H. 2018 Towards Adaptive Grids for Atmospheric Boundary-Layer Simulations. *Boundary-Layer Meteorology* **167** (3), 421–443.

VILLERMAUX, EMMANUEL & BOSSA, BENJAMIN 2009 Single-drop fragmentation determines size distribution of raindrops. *Nature Physics* **5** (9), 697–702.

ZHANG, B., LING, Y., TSAI, P.-H., WANG, A.-B., POPINET, S. & ZALESKI, S. 2019 Short-term oscillation and falling dynamics for a water drop dripping in quiescent air. *Physical Review Fluids* **4** (12), 123604.

ZRNIĆ, D., BERGLEZ, P. & BRENN, G. 2022 Weakly nonlinear shape oscillations of a Newtonian drop. *Physics of Fluids* **34** (4), 043103.

ZRNIĆ, D. & BRENN, G. 2021 Weakly nonlinear shape oscillations of inviscid drops. *Journal of Fluid Mechanics* **923**.